An error covariance correction-adaptive extended Kalman filter based on piecewise forgetting factor recursive least squares method for the state-of-charge estimation of lithium-ion batteries.

LIANG, Y., WANG, S., FAN, Y., TAKYI-ANINAKWA, P., XIE, Y. and FERNANDEZ, C.

2023

An error covariance correction-adaptive extended Kalman filter based on piecewise forgetting factor recursive least squares method for the state-of-charge estimation of lithium-ion batteries

Yawen Liang[b], Shunli Wang[a,b], Yongcun Fan[a], Paul Takyi-Aninakwa[a], Yanxin Xie[a], Carlos Fernandez[c]

[a]School of Information Engineering, Southwest University of Science and Technology, Mianyang, 621010, China;

[b]College of Electrical Engineering, Sichuan University, Chengdu, 610065, China;

[c]School of Pharmacy and Life Sciences, Robert Gordon University, Aberdeen, AB10-7GJ, UK.

Abstract: Accurate state-of-charge (SOC) estimation is essential for fully utilizing the battery performance of electric vehicles. Considering the demand for algorithms with the advantages of simplicity, fewer calculations, good stability, and high accuracy in practical applications, this paper proposes a novel error covariance correction-adaptive extended Kalman filter (ECC-AEKF) for accurate and robust SOC estimation. In this paper, the maximum likelihood function of the probability density function of the error series (conditional on the priori covariance) is calculated by mathematical derivation to obtain a new priori error covariance, which is used to obtain a more appropriate Kalman gain. The ECC-AEKF can minimize the estimation error and reduces the effect of process noise characteristics and inappropriate error covariances on priori estimates. Meanwhile, a piecewise forgetting factor recursive least square (PFFRLS) is presented for model parameter identification. The PFFRLS using error feedback for real-time adaptively adjusts the forgetting degree of data based on the principle of integral separation. Furthermore, a comparative analysis of SOC estimation in PFFRLS-ECC-AEKF and commonly used methods is presented for validation of the performance of the proposed method under different temperatures and operating conditions. The results prove that the PFFRLS-ECC-AEKF achieves higher accuracy with less computation time than other methods.

Keywords: State-of-charge; Adaptive extended Kalman filter; Lithium-ion batteries; Piecewise forgetting factor; Priori error covariance correction

***Corresponding author:** Shunli Wang. Tel:+186-15884655563. E-mail address: wangshunli@swust.edu.cn

1 Introduction

At present, the world is facing a serious situation of severe environmental damage and tightening resource constraints [1, 2]. The rise in crude oil prices has urged the development of alternative fuel-driven vehicles [3]. Therefore, the implementation of Electric Vehicles (EVs) has garnered tremendous attention, and its energy management has become an important development direction in the automobile industry [4]. As the main energy source of an EV, power batteries determine the cruising range, dynamic performance and use cost of the EV [5, 6]. Accurate state of charge (SOC) estimation of lithium-ion batteries in electric vehicles has many advantages, such as efficient vehicle-to-grid methods can be accurately established from SOC-related knowledge, SOC estimation can accurately estimate the range of the other battery states and system parameters, SOC accurate estimation can extend battery life and ensure the safety of the battery system, etc. [7]. At present, there have been some pioneering works on SOC estimation for lithium-ion batteries, which mainly include three main categories: direct calculation methods, model-based methods and data-driven methods [8].

In the first category, the more representative methods are the ampere-time integration method [9], the open-circuit voltage method [10] and the ultrasonic transmission method [11]. These methods are widely used in practice for their simplicity, low computational effort, stability and guaranteed accuracy [12]. For example, Yu et al. [13] experimentally obtained Open-circuit voltage (OCV) -SOC curves at different temperatures and aging stages, which were used to investigate the sensitivity of eighteen OCV battery models to ambient temperatures, aging stages, the amount of data and SOC region. However, these methods ignore battery internal variation and estimate SOC from a simple relationship between external parameters and SOC. Also, the direct calculation methods are extremely dependent on accurate OCV values and initial SOC values.

In the second category, the best-known methods involve Kalman Filter (KF) [14], Extended Kalman Filter (EKF) [15-17], Unscented Kalman Filter (UKF) [18, 19], Fading Kalman Filter (FKF) [20], Cubature Kalman Filter (CKF) [21, 22], Unscented Particle Filter (PF) [23], H-infinity Observer [24], Sliding Mode Observer (SMO) [25] and so on. They utilize the battery equivalent model to describe the state-space equations, which has the advantages of adaptively reducing the influence of noise characteristics, simple calculations, and high accuracy [26]. Liu et al. [27] proposed an improved CKF using Singular Value Decomposition (SVD) and a Forgetting Factor Recursive Least Square (FFRLS) with a Recursive Gradient Correction (RGC) strategy for high-precision SOC estimation. Takyi-Aninakwa et al. [28] propose a Strong Tracking Adaptive Fading-Extended Kalman Filter (STAF-EKF), which is capable of high accuracy SOC estimation at temperatures as low as -10°C. Lai et al. [29] combined a discrete Arrhenius Aging Model (DAAM) with a Sequential Extended Kalman filter (SEKF) to improve the accuracy and reliability of battery capacity estimation. Wei et al. [30] proposed a novel parameter identification method combining an Instrumental Variable (IV) and the bilinear principle to compensate for noiseinduced biases in the parameter identification of the battery model, and further parameterisation using the Luenberger Observer (LO). However, the estimation accuracy of those methods directly depends on the accuracy of the equivalent model and the influence of noise characteristics.

In recent years, the third category of methods has attracted a great deal of interest from many researchers [31], including Backpropagation Algorithm (BP) [32, 33], Support Vector Machine (SVM) [34], Long Short-Term Memory (LSTM) [35, 36], Gaussian process regression (GPR) [37], Multilayer Perceptron (MLP) [38], Hybrid Electrochemical-Thermal-Neural-Network model (ETNN) [39] and many others. These methods do not require consideration of the complex coupling relations between the estimated states and the influencing factors, and ignore the effects of model accuracy and noise characteristics [40]. Jiao et al. [41] trained the Regularized Extreme Learning Machine (RELM) with a Spectral Fletcher-Reeves (SFR) algorithm and used a Beetle Antenna Search algorithm (BAS-SFR-RELM) to parameterize the model for fast and accurate SOC estimation. Bian et al. [42] introduced a stacked multilayer and bidirectional recursive structure to the LSTM model to propose a Stacked Bidirectional Long Short-Term Memory (SBLSTM) model, which can accurately estimate the battery SOC exclusively using historical information. Lipu et al. [43] proposed an optimal nonlinear autoregressive with exogenous input (NARX) based on a neural network (NARXNN) and used a Lighting Search Algorithm (LSA) to find delayed values and hidden layer neurons to achieve accurate and robust SOC estimation. However, these approaches rely on a large amount of experimental data to train the Neural Network (NN), which is computationally intensive and requires a high level of equipment and has certain limitations in practical applications.

In summary, model-based approaches and data-driven approaches have been widely studied by many researchers for their high accuracy and robustness. However, in practical vehicle applications, considering the economic cost, calculation and overall efficiency, the look-up table method and KF-based method are most often used for battery SOC estimation, which are simple and practical, with fewer calculations, good stability and suitable accuracy [44]. Even so, to facilitate the rapid development of the new energy industry, traditional simple algorithms do not meet the needs of further practical production applications [45]. It is crucial to strike a balance between traditional methods and optimal algorithms so that the optimization algorithms are also applicable to practical applications while taking into account realistic issues. Therefore, this paper chooses to optimize the model-based methods which have the advantages of low computational effort, good stability and high accuracy.

Considering the importance of model accuracy and noise characteristics to model-based methods. If these two factors are incorrectly set, the estimation error will be large or even divergent [46]. Among them, the accuracy of the equivalent model is closely related to its complexity, and the noise characteristics are related to the model uncertainty and measurement error [47]. According to [48], the model uncertainty proved to be inevitable. Measurement deviations are generally caused by external disturbances and sensor deviations. Therefore, the Kalman gain is closely related to the noise covariance and error covariance. The key is to accurately characterize the coupling between the noise covariance and error covariance to obtain a suitable Kalman gain to estimate the accurate battery SOC and reduce the estimation errors.

To obtain high-precision state parameters of lithium-ion batteries. in this paper, a new priori error covariance is obtained by mathematical derivation to optimize the widely used EKF, and then a novel error covariance correction-adaptive extended Kalman filtering (ECC-AEKF) is proposed. The ECC-AEKF can minimize the estimation error without directly considering the effect of process noise characteristics and reduces the impact of inappropriate error covariances on priori estimation. Specifically, this paper solves the maximum likelihood function of the probability density function of the error series (conditional on the priori covariance) by mathematical derivation, to find a new coupling relationship between the priori error covariance and the state covariance. In addition, the priori error covariance of the ECC-AEKF can be adaptively selected according to the estimation effect, resulting in a more appropriate Kalman gain for better battery SOC estimation. Meanwhile, since the selection of different forgetting factors directly affects the effectiveness of parameter identification and the discrimination of model accuracy. To solve the issue that a fixed forgetting factor will reduce the accuracy, stability and topicality of the parameter identification. Therefore, a piecewise forgetting factor recursive least square (PFFRLS) is presented for model parameter identification, which uses error feedback for real-time adaptive selection of the forgetting factors based on the principle of integral separation. Ultimately, the PFFRLS-ECC-AEKF method is used for accurate and robust SOC estimation. The accuracy, efficiency and robustness of the proposed method are evaluated under HPPC, BBDST and DST operating conditions at different ambient temperatures, and a comparative analysis of the proposed method with commonly used SOC estimation methods is carried out. The results prove that the PFFRLS-ECC-AEKF achieves higher accuracy with less computation time than other widely used SOC estimation methods under different ambient temperatures and drive cycles. The proposed method has the advantages of simplicity of use, low computational effort and good stability of the EKF, as well as the advantages of high accuracy and robustness of the optimization algorithm, and also bringing the possibility of obtaining more accurate SOC estimates for practical applications.

2 Battery modeling

2.1 Second-order RC circuit network model

Establishing a battery equivalent circuit model is the premise for the SOC estimation of lithium-ion batteries [49]. Typical battery circuit models are mainly divided into electrochemical models (EM), equivalent circuit models (ECM) and NN models [50]. Among them, ECM-based methods have been widely used because of their moderate computation and good accuracy, which are divided into the integer-order model [51] and the fractional-order model [52]. The complexity, modeling accuracy and difficulty of these two types of models increase in descending order [53]. This paper considers the process of ohmic voltage drop, polarization and expansion inside the actual lithium-ion batteries, and chooses to add a capacitor-resistance (RC) loop based on the Thevenin model, which can better express the static and dynamic characteristics of the batteries, thus improving the accuracy of battery SOC estimation. This equivalent circuit model applies to most types of batteries and meets the requirements of the model for accuracy, complexity, and computational complexity. The second-order RC network model is shown in Figure 1.

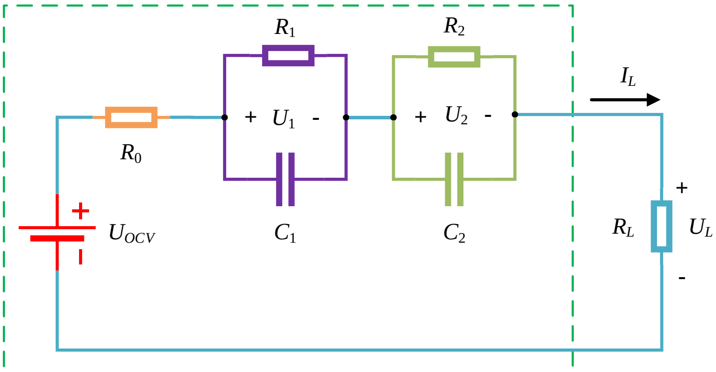

Figure 1. Second-order RC network model

As shown in Figure 1, R_0 is the internal resistance of the lithium-ion battery; R_1 and R_2 are the electrochemical polarization internal resistance and the concentration polarization internal resistance, respectively; C_1 and C_2 are the electrochemical polarization capacitance and concentration polarization capacitance, respectively; R_1C_1 characterizes the charge change of the electric double layer of the power battery, and the voltage at both sides is the interface overpotential U_1; R_2C_2 characterizes the diffusion phenomenon of the battery, which is equivalent to an RC loop, and the voltage of which is the cross-interface potential U_2; U_{OCV} and U_L are the output voltage and load current of the battery, respectively.

2.2 Model-based state space representation

According to Kirchhoff's circuit law, circuit physical quantities can be described as

$$\begin{cases} U_L = U_{OCV}(SOC) - I_L R_0 - U_1 - U_2 \\ I_L = C_1 \dfrac{dU_1}{dt} + \dfrac{U_1}{R_1} = C_2 \dfrac{dU_2}{dt} + \dfrac{U_2}{R_2} \end{cases} \tag{1}$$

Equation (1) is transformed into Equation (2) by projecting it into the discrete time domain.

$$\begin{cases} U_1(t) = \exp(-T_s / R_1C_1)U_1(t-T_s) + (1-\exp(-T_s / R_1C_1))R_1 I_L(t-T_s) \\ U_2(t) = \exp(-T_s / R_2C_2)U_2(t-T_s) + (1-\exp(-T_s / R_2C_2))R_2 I_L(t-T_s) \end{cases} \tag{2}$$

where T_s is the sampling time of the parameter estimator. The recursive formula for the lithium-ion batteries SOC is calculated by the ampere-hour integration in the discrete-time domain as follows

$$SOC_k = SOC_{k_0} - \frac{\eta}{C}\int_0^k I(k)dk \tag{3}$$

Where SOC_{k0} is the initial value of the battery SOC estimation; C is the battery capacity; η is the Coulombic efficiency during charging and discharging. Combining Equation (2) and Equation (3), the state-space equation of the ECM can be obtained

$$x_k = \begin{pmatrix} SOC_k \\ U_{1,k} \\ U_{2,k} \end{pmatrix} = \begin{pmatrix} 1 & 0 & 0 \\ 0 & \exp(-T_s/\tau_1) & 0 \\ 0 & 0 & \exp(-T_s/\tau_2) \end{pmatrix} \begin{pmatrix} SOC_{k-1} \\ U_{1,k-1} \\ U_{2,k-1} \end{pmatrix} + \begin{pmatrix} -\eta T_s / C \\ R_1(1-\exp(-T_s/\tau_1)) \\ R_2(1-\exp(-T_s/\tau_2)) \end{pmatrix} I_k + \begin{pmatrix} w_{1,k} \\ w_{2,k} \\ w_{3,k} \end{pmatrix} \tag{4}$$

$$z_k = U_{L,k} = U_{OCV,k} - R_0 I_k + \begin{pmatrix} 0 \\ -1 \\ -1 \end{pmatrix}^T \begin{pmatrix} SOC_k \\ U_{1,k} \\ U_{2,k} \end{pmatrix} + v_k \tag{5}$$

Where $U_{1,k}$ and $U_{2,k}$ are the voltages flowing through the polarized capacitors C_1 and C_2, respectively; $U_{L,k}$ and $U_{OCV,k}$ are the battery terminal voltage and open-circuit voltage, respectively; I_k is the main circuit current; w_k and v_k are the process noise and measurement noise, respectively, which are uncorrelated zero-mean Gaussian white noise. The nth-order polynomial fitting function OCV of SOC is expressed as

$$U_{OCV} = \psi(SOC) = \sum_{i=0}^{n} a_i (SOC)^i \tag{6}$$

where the fitting coefficient a_i can be obtained from a polynomial fitting of data through MATLAB.

From Equations (4)–(6), the state equation and observation equation of a nonlinear discrete system are expressed by

$$\begin{cases} x_k = A_k x_{k-1} + B_k u_{k-1} + \omega_k = f(x_{k-1}, u_{k-1}) + w_k \\ y_k = C_k x_k + D_k u_k + \upsilon_k = h(x_k, u_k) + v_k \end{cases} \tag{7}$$

where x_k and y_k are the state variables and measurement variables of the system at time k, respectively; u_k is the input variable of the system at time k; A_k, B_k, C_k and D_k are the state transition matrix, input matrix, output matrix and feedforward matrix, respectively. From Equations (4)-(5) and (7), the state variable x_k of the filter algorithm can be defined as

$$x_k = [SOC_{k+1}, U_{1,k+1}, U_{2,k+1}]^T \tag{8}$$

Through calculation, Equations (9)-(10) are obtained.

$$A_k = \begin{pmatrix} 1 & 0 & 0 \\ 0 & \exp(-T_s/\tau_1) & 0 \\ 0 & 0 & \exp(-T_s/\tau_2) \end{pmatrix} \tag{9}$$

$$B_k = \left[-\frac{\eta T_s}{C}, R_1(1-\exp(-T_s/\tau_1)), R_2(1-\exp(-T_s/\tau_2)) \right]^T \tag{10}$$

$$\begin{cases} C_k = \left[\left. \dfrac{\partial U_{OCV}(soc_k)}{\partial soc_k} \right|_{SOC_k = SOC_k} \quad -1 \quad -1 \right] \\ D_k = -R_0 \end{cases} \tag{11}$$

where $U_k = I_k$, $y_k = U_{L,k}$, $\widehat{SOC}_k$ is the predicted value of SOC_k. The fitting OCV and SOC curve is shown in Figure 2.

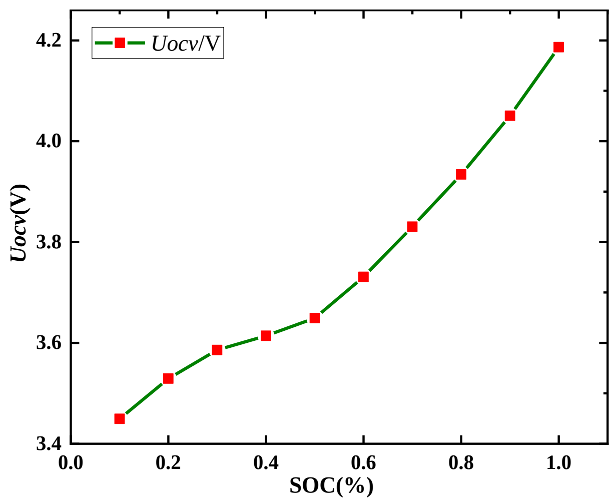

Figure 2. Function fitting curve of open-circuit voltage and SOC

3 SOC estimation methods development

3.1 Forgetting factor recursive least squares method

The model-based approaches are greatly dependent on the accuracy of the ECM, and the variable model parameters affect SOC estimation. Therefore, it is crucial to use a suitable method to accurately calculate the model parameters. The frequency domain expression of Equation (1) can be written as

$$U_{OCV}(s) - U_L(s) = I(s)\left(\frac{R_1}{1+\tau_1 s} + \frac{R_2}{1+\tau_2 s} + R_0\right) \tag{12}$$

where $\tau_1 = R_1C_1$ and $\tau_2 = R_2C_2$ are the time constants. Then, the transfer function of Equation (12) can be written as

$$G(s) = \frac{Y(s)}{I(s)} = \frac{U_{OCV}(s) - U_L(s)}{I(s)} = \frac{R_0\tau_1\tau_2 s^2 + (R_0\tau_1 + R_0\tau_2 + R_1\tau_2 + R_2\tau_1)s + (R_0 + R_1 + R_2)}{\tau_1\tau_2 s^2 + (\tau_1 + \tau_2)s + 1} \tag{13}$$

The bilinear transformation equation $s = \frac{2}{T} \cdot \frac{1-z^{-1}}{1+z^{-1}}$ is used to discretize Equation (13), and obtain its discrete transfer function as

$$G(z^{-1}) = \frac{Y(k)}{I(k)} = \frac{a_3 + a_4 z^{-1} + a_5 z^{-1}}{1 - a_1 z^{-1} - a_2 z^{-2}} \tag{14}$$

Then, the difference equation form of Equation (14) is obtained as

$$Y(k) = a_1Y(k-1) + a_2Y(k-2) + a_3I(k) + a_4I(k-1) + a_5I(k-2) \tag{15}$$

where $a_1 \sim a_5$ are unknown coefficients, from which the parameters of the second-order RC network model can be derived. The single in- output process described by a generic higher-order autoregressive system is shown below

$$Y(k) = \phi(k)\theta^T + \delta(k) \tag{16}$$

where δ is zero-mean random noise. Suppose that b_1, b_2, b_3, b_4, b_5 are

$$\begin{cases} b_1 = R_0 \\ b_2 = \tau_1\tau_2 \\ b_3 = \tau_1 + \tau_2 \\ b_4 = R_0 + R_1 + R_2 \\ b_5 = R_0\tau_1 + R_0\tau_2 + R_1\tau_2 + R_2\tau_1 \end{cases} \tag{17}$$

Substituting Equation (17) into Equation (14) yields

$$\begin{cases} b_1 = -(a_3 - a_4 + a_5) / (1 + a_1 - a_2) \\ b_2 = T^2(1 + a_1 - a_2) / 4(1 - a_1 - a_2) \\ b_3 = T(1 + a_1) / (1 - a_1 - a_2) \\ b_4 = -(a_3 + a_4 + a_5) / (1 - a_1 - a_2) \\ b_5 = T(a_5 - a_3) / (1 - a_1 - a_2) \end{cases} \tag{18}$$

where T is the sample time. By the above calculation, the parameter of the ECM can be expressed as

$$\begin{cases} R_0 = b_1 \\ R_1 = [\tau_1(b_4 - b_1) + b_1b_3 - b_5] / (\tau_1 - \tau_2) \\ C_1 = \tau_1 / R_1 \\ R_2 = b_4 - (R_0 + R_1) \\ C_2 = \tau_2 / R_2 \end{cases} \tag{19}$$

The real-time parameters of the ECM can be obtained by analyzing the discharge terminal voltage of the lithium-ion batteries, along with the above derivation process and the input experimental data.

3.2 Optimized piecewise forgetting factor strategy

The forgetting factor is mainly utilized to increase the weight of new data, thereby enhancing the adaptability to non-stationary signals. It characterizes the ability of the adaptive filter to quickly reflect changes in the input characteristics. According to Equation (20), when the forgetting factor is large, the historical data account for a large, but it cannot track the changes of system parameters in real-time. When the forgetting factor is small, the historical data are easily forgotten to a large extent, and the tracking output changes are better, but the stability is poor. Therefore, the forgetting factor is generally between 0.95 and 0.995 according to previous research [54]. To sum up, a single forgetting factor cannot precisely implement the model identification process in a system with time-varying parameters.

$$J = \sum_{j=1}^{N} \lambda^{N-j}[e(j)]^2 = [e(j)]^2 + \lambda[e(j-1)]^2 + \lambda^2[e(j-2)]^2 + \cdots + \lambda^{N\text{-}1}e^2 \tag{20}$$

According to the characteristics of different sizes of forgetting factors, it can be regarded as the integration link in proportional integral differential (PID) regulation. Therefore, a piecewise forgetting factor recursive least-squares (PFFRLS) method based on integral separation is used in this paper, which can segment the forgetting factors according to the absolute error between the current estimated output and the actual output. When the error is large, the integral action is canceled to avoid reducing the stability of the system. When the error is small, the integral action is introduced to eliminate the net difference and improve the control accuracy. Searching for several error points $\vartheta_1, \vartheta_2, \cdots \vartheta_n$ in the range of absolute errors, and when the error range is $[\vartheta_i, \vartheta_{i+1}]$, it corresponds to forgetting factors $\lambda = \lambda_i,\ i = 1,2,\cdots,n$, respectively. The error point ϑ_i is obtained by the error feedback from the previous round of parameter identification. The number and size of ϑ_i depend on the actual estimation effect. Generally, the first error point is taken to be $\vartheta_1 = 0$ and the last error point ϑ_n should be slightly smaller than the maximum absolute error. A correction function λ is given as

$$\lambda = \begin{cases} \lambda_1, \vartheta_1 \le |e| < \vartheta_2 \\ \lambda_2, \vartheta_2 \le |e| < \vartheta_3 \\ \vdots \\ \lambda_i, \vartheta_{i-1} \le |e| < \vartheta_i \end{cases} \tag{21}$$

From Equation (21), the forgetting factor is adaptively adjusted by the absolute error between the current estimated output and the actual output. When the absolute error is large, a smaller forgetting factor should be selected to improve the tracking speed of the estimated parameters when the parameters are abruptly changed.

When the absolute error is small, a larger forgetting factor should be selected, so that the parameters have better steady-state performance. The purpose of the PFFRLS algorithm is to accurately value the forgetting factors in real-time, to provide the system with better stability and accuracy. The flowchart of the PFFRLS algorithm is shown in Table 1.

Table 1. The flowchart of the PFFRLS algorithm

Step 1. Initialize estimation parameter and error posterior covariance at step $k = 0$.

$$\hat{\theta}(0) = E(\theta(0)) \tag{22}$$

$$P(0) = E[(\theta(0) - \hat{\theta}(0))(\theta(0) - \hat{\theta}(0))^T] \tag{23}$$

Step 2. Update priori estimation parameters and covariance.

$$\hat{\theta}(k) = \hat{\theta}(k-1) \tag{24}$$

$$P(k) = P(k) \tag{25}$$

Step 3. Update algorithm gain.

$$L(k+1) = P(k)\varphi(k)[\lambda + \varphi^T(k)P(k)\varphi(k)]^{-1} \tag{26}$$

Step 4. Update output prediction and estimation error.

$$E(k) = \theta^T(k-1)\varphi(k) \tag{27}$$

$$e(k) = y(k+1) - \varphi^T(k+1)\hat{\theta}(k) \tag{28}$$

Step 5. Update posteriori estimation parameters and covariance.

$$\hat{\theta}(k+1) = \hat{\theta}(k) + L(k+1)e(k+1) \tag{29}$$

$$P(k+1) = \lambda^{-1}[P(k) - L(k)\varphi^T(k)P(k)] \tag{30}$$

Among them, the piecewise forgetting factor is introduced and calculated as follows.

$$\lambda = \begin{cases} \lambda_1, \vartheta_1 \le |e| < \vartheta_2 \\ \lambda_2, \vartheta_2 \le |e| < \vartheta_3 \\ \vdots \\ \lambda_i, \vartheta_{i-1} \le |e| < \vartheta_i \end{cases} \tag{31}$$

3.3 Error covariance correction-adaptive extended Kalman filter

The ordinary EKF algorithm is used to deal with the estimation problem of a nonlinear system that is closely related to the system noise characteristics. Compared to many improved filtering algorithms and artificial intelligence algorithms, the EKF is widely used in practical engineering because of its affordability, easy to use, and acceptable error. The detailed steps of the EKF can be summarized as follows:

Step 1. Initialize state variable and error covariance matrix at step $k = 0$.

$$\begin{cases} x_0 = E\left[x_0\right] \\ P_0 = E\left[(x_0 - x_0)(x_0 - x_0)^T\right] \end{cases} \tag{32}$$

where $\hat{x}_0$ and P_0 are the estimated initial state variable and error covariance matrix.

Step 2. Update the predicted estimates of the state variables and the error covariance.

$$x_{k|k-1} = f(x_{k-1|k-1}, u_{k-1}) \tag{33}$$

$$P_{k|k-1} = A_{k-1}P_{k-1|k-1}A_{k-1}^T + Q_k \tag{34}$$

Step 3. Calculate the Kalman gain.

$$L_k = P_{k|k-1}C_k^T(C_kP_{k|k-1}C_k^T + R_k)^{-1} \tag{35}$$

where Q_k and R_k are the covariances of the process noise ω_k and the measurement noise v_k, respectively.

Step 4. Perform optimal estimation of the state variables and the error covariance.

$$x_{k|k} = x_{k|k-1} + L_k\left[y_k - g(x_{k|k-1}, u_k)\right] \tag{36}$$

$$P_{k|k} = (E - K_kC_k)P_{k|k-1} \tag{37}$$

However, the EKF still has some limitations. There is a truncation error in the linearization process due to replacing the infinite Taylor calculation process with a finite one. However, truncation error is an unavoidable method error inherent in numerical calculation methods. In addition, the filter assumes the system noise has a fixed white Gaussian noise. However, the statistical characteristics of the battery system noise are unknown, which will result in a large estimation error in practical application. Furthermore, arbitrary adjustments of the noise covariance may over- or underestimate the measured values, leading to stable divergence or too noisy filter behavior, respectively. In the latter and worst conditions, the filter estimate becomes an open-loop prediction process since the Kalman gain is minimized. Similarly, if the initial value is set unreasonably, divergence occurs.

The noise covariance Q_k and R_k are usually kept constant to meet the real-time requirements of the BMS, which greatly affect the filter response. They make the filtering algorithm include a large amount of uncertainty to cover erroneous initial value, error or noise, and model inaccuracies. With this general analysis at hand, it is necessary to try to avoid the effect of artificially adjusted noise covariance on the error covariance and to reset a novel priori error covariance that is unaffected by the noise characteristics to obtain a more appropriate Kalman gain, so that the SOC estimation results can be optimized.

In this paper, we consider minimizing the error objective function and establishing a conditional probability density function for the error sequence conditional on the priori error covariance to seek the coupling between both. In addition, a new priori error covariance characterized by the state variables is obtained by solving the maximum likelihood function of this probability density function, and then the ECC-AEKF method is proposed. The specific steps are shown below.

In this optimal adaptive estimator, the error sequence is the crucial data used to adaptively update the ECM parameters, which is defined by

$$e_k = y_k - h(\hat{x}_{k|k-1}, u_k) \tag{38}$$

We expand e_k into the set of error sequences from time i_0 to $k-1$ as given by

$$\xi_k = \{e_{i_0}, e_{i_0+1}, \cdots, e_{k-1}\} \tag{39}$$

where $e_{i_0}, e_{i_0+1}, \cdots, e_{k-1}$ are independent of each other, k is the total length of time and i is the length of time of the error sequence.

If the parameters of the lithium-ion batteries change slowly during the system operation and the filter can be initialized correctly, and the priori error covariance is convergent. Therefore, the estimation of the priori error covariance can be corrected in real-time by finding a local optimal but explicit and efficient way. $\hat{P}_{k|k-1}$ represent the estimated value of the priori error covariance $P_{k|k-1}$, as well as $p(\xi_k \left| \hat{P}_{k|k-1}\right.)$ represent the probability density function of the historical error sequence ξ_k conditional on the priori covariance $\hat{P}_{k|k-1}$. $p(\xi_k \left| \hat{P}_{k|k-1}\right.)$ can be transformed into the probability density function of the error sequence e_k conditional on the priori covariance $\hat{P}_{k|k-1}$ as expressed by

$$p(\xi_k \left| \hat{P}_{k|k-1}\right.) = \frac{p(\xi_k)}{p(\hat{P}_{k|k-1})} = \frac{p(\{e_{i_0}, e_{i_0+1}, \cdots, e_{k-1}\})}{p(\hat{P}_{k|k-1})} = \prod_{i=i_0}^{k-1} p(e_i \left| \hat{P}_{k|k-1}\right.) \tag{40}$$

Next, the maximum likelihood function of $\hat{P}_{k|k-1}$ can be expressed as

$$L(\hat{P}_{k|k-1}) = \ln p(\xi_k \left| \hat{P}_{k|k-1}\right.) = \sum_{i=i_0}^{k-1} \ln p(e_i \left| \hat{P}_{k|k-1}\right.) \tag{41}$$

Then, the logarithm of the probability density function can be extended to

$$\ln p(e_i \left| \hat{P}_{k|k-1}\right.) = \ln p(e_i \left| \hat{P}_{i|i-1}\right.) = -\frac{[\ln(2\pi)^n + \ln\left| I_{e_i}\right| + e_i^T I_{e_i}^{-1} e_i]}{2} \tag{42}$$

where n is the measurement number; I_{e_i} is the covariance matrix associated with the error sequence e_k. In order to make Equation (41) effective as well as simplify its calculation, the evaluation factor of Equation (42) is taken

$$MAX_k = \sum_{i=i_0}^{k-1}(\ln\left|I_{e_i}\right| + e_i^T I_{e_i}^{-1} e_i) \tag{43}$$

Since $I_{e_i} = I_i P_{k|k-1} I_i^T + R$. We now find the maximum likelihood function of the evaluation factor, and make its derivative value equal to zero, which is expressed as

$$L(MAX_K) = \sum_{i=i_0}^{k-1}[tr(I_{e_i}^{-1} I_i \frac{\partial P_{i|i-1}}{\hat{P}_{k|k-1}} I_i^T) - e_i I_{e_i}^{-1} I_i \frac{\partial P_{i|i-1}}{\hat{P}_{k|k-1}} I_i^T I_{e_i}^{-1} e_i^T] = 0 \tag{44}$$

With the gradual iteration of the EKF algorithm, the estimation error converges to zero. During the same time, the priori error covariance $P_{k|k-1}$ converges rapidly, that is, a constant approximation. Meanwhile, $\frac{\partial P_{i|i-1}}{\hat{P}_{k|k-1}}$ is approximately equal to the identity matrix I. Equation (44) can be transformed into

$$L(MAX_K) = \sum_{i=i_0}^{k-1}[tr(I_{e_i}^{-1} I_i I_i^T) - e_i I_{e_i}^{-1} I_i I_i^T I_{e_i}^{-1} e_i^T] = 0 \tag{45}$$

For Equation (45) to hold, Equation (46) must be satisfied.

$$tr(I_{e_i}^{-1} I_i I_i^T) - e_i I_{e_i}^{-1} I_i I_i^T I_{e_i}^{-1} e_i^T = 0 \tag{46}$$

From Equation (28) and Equation (38), it can be known that I_{e_i} and e_i are 1×1 matrix. Thereupon, Equation (46) can be transformed into

$$P_{i|i-1} I_i^T (I_{e_i}^{-1} - I_{e_i}^{-1} e_i e_i^T I_{e_i}^{-1}) I_i P_{i|i-1} = 0 \tag{47}$$

Since $(I_{e_i}^{-1})^T = I_{e_i}^{-1}$, and $P_{i|i-1}$ is a symmetric positive definite matrix, substituting Equation (35) into Equation (47) yields

$$L_i (I_i P_{i|i-1} - e_i e_i^T L_i^T) = 0 \tag{48}$$

Let increment $\Delta\hat{x}_i = \hat{x}_i - \hat{x}_{i|i-1} = L_i e_i$, and Equation (37) is $P_{i|i} = (I - L_i C_i) P_{i|i-1}$ at time i. Substituting them into Equation (48) yields

$$P_{i|i-1} = P_{i|i} + \Delta\hat{x}_i \Delta\hat{x}_i^T \tag{49}$$

Then Equation (49) is transformed into the form of accumulating from time i_0 to $k-1$, as shown by

$$\sum_{i=i_0}^{k-1} P_{i|i-1} = \sum_{i=i_0}^{k-1}(P_{i|i} + \Delta\hat{x}_i \Delta\hat{x}_i^T) \tag{50}$$

Assuming the approximate value $P_{k|k-1} = P_{i|i-1}, (i < k)$, then the estimated covariance $P_{k|k-1}$ can be approximated as the average value of $P_{i|i-1}$ from time i_0 to $k-1$, as shown by

$$\hat{P}_{k|k-1} = \left(k - i_0\right)^{-1} \sum_{i=i_0}^{k-1} P_{i|i-1} = \left(k - i_0\right)^{-1} \sum_{i=i_0}^{k-1} (P_{i|i} + \Delta\hat{x}_i \Delta\hat{x}_i^T) \tag{51}$$

Similarly, the estimated covariance $P_{k-1|k-2}$ is calculated by

$$\hat{P}_{k-1|k-2} = \left(k - 1 - i_0\right)^{-1} \sum_{i=i_0}^{k-2} P_{i|i-1} = \left(k - 1 - i_0\right)^{-1} \sum_{i=i_0}^{k-2} (P_{i|i} + \Delta\hat{x}_i \Delta\hat{x}_i^T) \tag{52}$$

Furthermore, the recursive calculation of $P_{k|k-1}$ is calculated by

$$\hat{P}_{k|k-1} = \left(k - i_0\right)^{-1} [\hat{P}_{k-1|k-1} + \Delta\hat{x}_{k-1} \Delta\hat{x}_{k-1}^T + (k - 1 - i_0)\hat{P}_{k-1|k-2}] \tag{53}$$

Substituting Equation (37) into Equation (53), the recursive formula for estimating the priori error covariance $\hat{P}_{k|k-1}$ can be obtained.

$$\hat{P}_{k|k-1} = \hat{P}_{k-1|k-2} + \frac{\Delta\hat{x}_{k-1} \Delta\hat{x}_{k-1}^T - L_{k-1} C_{k-1} \hat{P}_{k-1|k-2}}{k - i_0} \tag{54}$$

Combining Equation (34) with Equation (54), and taking the filter convergence time k_0 as the segment point, we obtain the final priori error covariance recursion formula.

$$\begin{cases} \hat{P}_{k|k-1} = A_{k-1} P_{k-1|k-1} A_{k-1}^T + Q_{k-1}, k \le k_0 \\ \hat{P}_{k|k-1} = \hat{P}_{k-1|k-2} + (k - i_0)^{-1} (\Delta\hat{x}_{k-1} \Delta\hat{x}_{k-1}^T - L_{k-1} C_{k-1} \hat{P}_{k-1|k-2}), k > k_0 \end{cases} \tag{55}$$

The complete flowchart of the ECC-AEKF algorithm includes Equations (32), (33), (35)–(37), and (55), which are shown in Table 2.

Table 2. The flowchart of the ECC-AEKF algorithm

Step 1. Initialize state variable x_k and error covariance matrix P.
$\begin{cases} x_0 = E\left[x_0\right] \\ P_0 = E\left[(x_0 - x_0)(x_0 - x_0)^T\right] \end{cases}$
Step 2. Update the predicted estimates of the state variables.
$x_{k\|k-1} = f(x_{k-1\|k-1}, u_{k-1})$
Step 3. Update the predicted estimates of the state covariance at the filter convergence time k_0.
$\begin{cases} \hat{P}_{k\|k-1} = A_{k-1} P_{k-1\|k-1} A_{k-1}^T + Q_k, k \le k_0 \\ \hat{P}_{k\|k-1} = \hat{P}_{k-1\|k-2} + (k - i_0)^{-1} (\Delta\hat{x}_{k-1} \Delta\hat{x}_{k-1}^T - L_{k-1} C_{k-1} \hat{P}_{k-1\|k-2}), k > k_0 \end{cases}$
Step 4. Calculate the Kalman gain.
$L_k = P_{k\|k-1} C_k^T (C_k P_{k\|k-1} C_k^T + R_k)^{-1}$
Step 5. Perform optimal estimation of state variables.

$$x_{k|k} = x_{k|k-1} + L_k \left[y_k - g(x_{k|k-1}, u_k) \right]$$

Step 6. Perform optimal estimation of the error covariance.

$$P_{k|k} = (E - K_k C_k) P_{k|k-1}$$

The ECC-AEKF algorithm obtains the functional relationship between the feedback information $\Delta\hat{x}_i$ and the priori error covariance $P_{k|k-1}$ through the maximum likelihood method. The new priori error covariance can not only avoids the effect of noisy characteristics but also reduces the effect of inappropriate error covariance on the priori estimation. This covariance uses the state information from the previous moment to correct the current value to obtain a more appropriate Kalman gain to conduct accurate and robust SOC estimation. In addition, the statistical characteristics of the process noise can be indirectly estimated to reduce the effect of artificially adjusted noise covariance on the a priori error covariance. Furthermore, the new priori error covariance constructed is predicated on the minimization of the error objective function and the convergence of the filter, and hold at time k_0 when the filter first converges to zero, which is used to correct the Kalman gain after time k_0, so that the estimate values follow the true values as closely as possible, as well as the accuracy and robustness of the battery SOC estimate is improved.

3.4 Framework of SOC estimation approach

Figure 3 illustrates the flowchart of battery SOC estimation using PFFRLS-ECC-AEKF method. The left of Figure 3 shows the process of ECM parameter estimation using PFFRLS method, and the right of that one shows the iterative calculation process of battery SOC estimation using the ECC-AEKF algorithm.

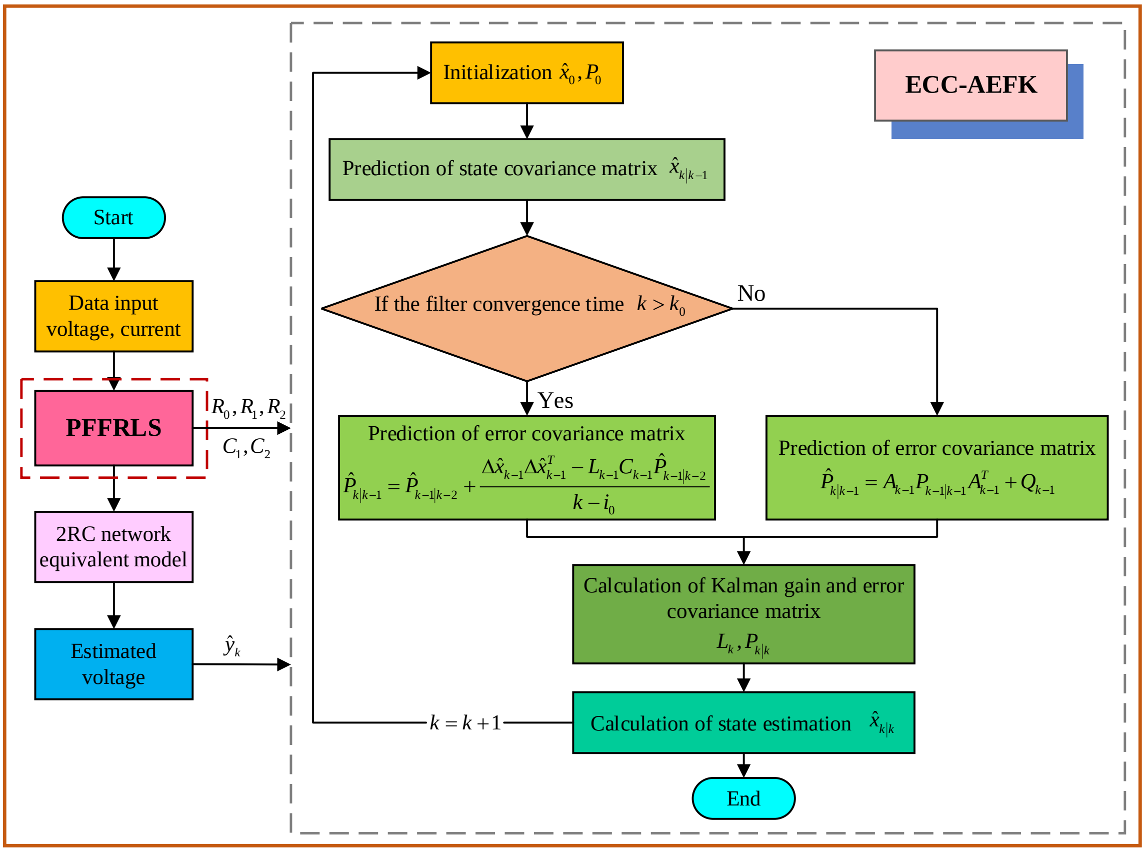

Figure 3. The flowchart of the SOC estimation with the proposed method

The ECC-AEKF algorithm has some limitations. Its derivation is suboptimal on the premise that the priori error covariances of the battery SOC estimation are approximate in the steady state. In addition, the experiment did not take into account the effects of battery aging. However, this experiment shall be used as a simulated attempt to study the reliability of battery SOC estimation under conditions where accurate noise parameters are not available and applications, so as to further avoid the failure of Kalman gain due to over- or underestimation of noise covariance. In practice, it is difficult to obtain the accurate noise parameters of the state equation and the observation equation for the battery system, so the optimal estimation cannot be achieved. The proposed method shall be seen as an alternative to the limitation mentioned above.

4 Experiments and discussion

4.1 Description of experiment data

A 3.7 V/70 Ah ternary lithium-ion battery was selected as the test object, with the specification shown in Table 3. The Neware battery test equipment is the CT-4016-5V100A-NTFA. The constant temperature box is a DGBELL BTT-331C. The experimental platform of the lithium-ion battery test equipment is shown in Figure 4.

Table 3. The specification of the 3.7 V/70 Ah ternary lithium-ion battery

Parameter	Value	Parameter	Value

Cell nominal capacity (Ah)	70	Peak discharge current	3 C
Cell nominal voltage (V)	3.7	Maximum load current	2 C
Charge cut-off voltage (V)	4.5±0.05	Internal resistance (mΩ)	0.5–1
Discharge cut-off voltage (V)	2.75±0.05	Working temperature (°C)	20~60
Standard charge current	1 C	Dimension: l×w×h (mm)	148×27×93

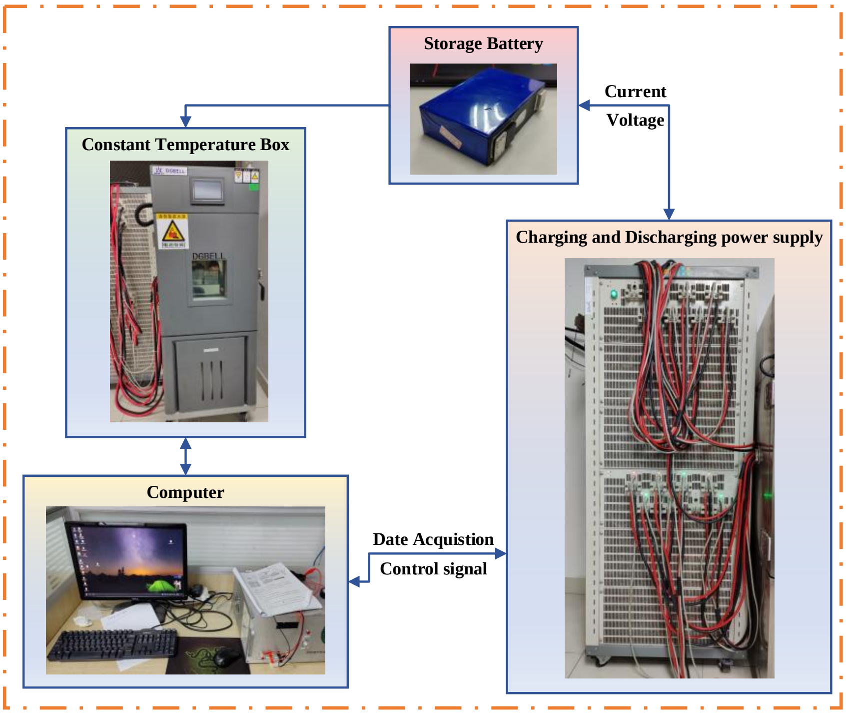

Figure 4. The experimental platform of lithium-ion battery test equipment

4.2 Battery model verification

4.2.1 HPPC operating condition

The hybrid pulse power characterization (HPPC) experiment records the battery SOC value, the open-circuit voltage and the main circuit current of the analog circuit under the current state by performing regular charge and discharge experiments on the analog circuit. The HPPC experiment was conducted as follows. Firstly, the lithium-ion battery was discharged for 10 s, then charged for 10 s after standing for 40 s, and finally left for 40 s. The whole process used 1 C to perform intermittent constant current discharge on the lithium-ion battery.

In this experiment, the forgetting factor λ of the FFRLS algorithm was chosen to be 0.99, 0.98, and 0.97 respectively. In addition, the current is used as input to the battery model to obtain the terminal voltage of its output. Figure 5 shows the experimental results of the FFRLS algorithm ($\lambda = 0.99$) and the PFFRLS algorithm under the HPPC operating condition.

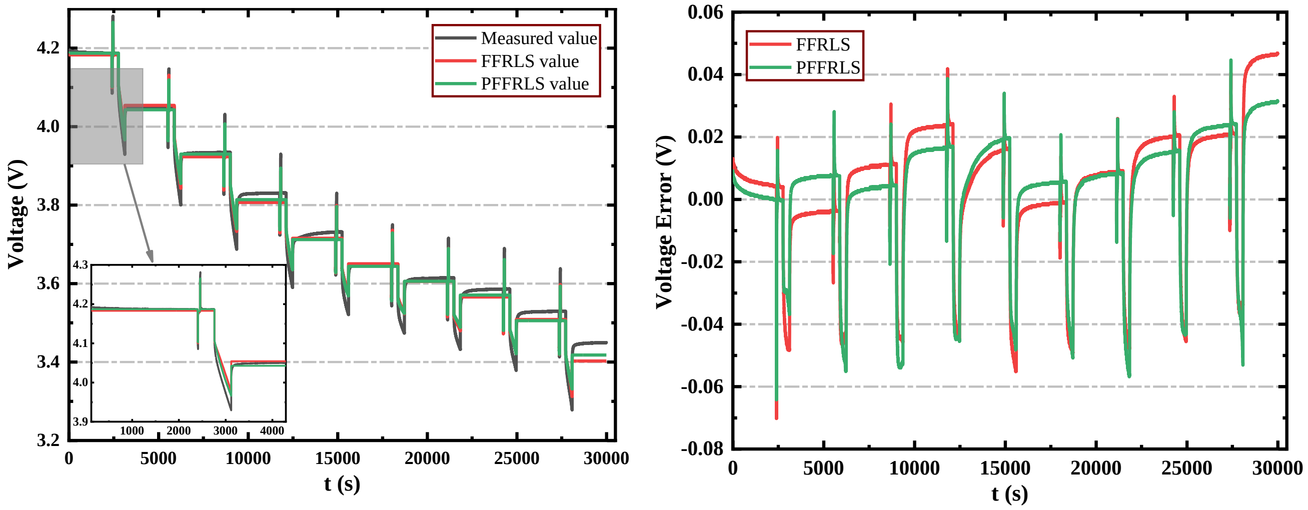

(a) Terminal voltage estimation results (b) Terminal voltage estimation errors

Figure 5. Identification results

322 The errors between the estimated terminal voltage and the actual terminal voltage of the ECM were compared, and the accuracy of the identification algorithm was analyzed, with the MaxAE, MAE and RMSE metrics shown in Table 4.

Table 4. Error evaluation of identification results

Identification methods	MaxAE (%)	MAE (%)	RMSE (%)
Single forgetting factor ($\lambda = 0.99$)	7.023	1.642	1.920
Single forgetting factor ($\lambda = 0.98$)	11.034	1.878	2.130
Single forgetting factor ($\lambda = 0.97$)	14.813	2.210	2.320
PFFRLS	6.410	1.430	1.878

Figure 5 and Table 4 indicate that the discriminant accuracy of the PFFRLS algorithm is higher than that of the FFRLS algorithm with a single forgetting factor, and the MaxAE, MAE and RMSE under the HPPC operating condition are 6.410%, 1.430% and 1.878%, respectively. The recognition error for every single forgetting factor differs little. By contrast, the single forgetting factor requires the artificial adjustment of parameters, which is time-consuming, labor-intensive, and difficult to accurately control the value. Therefore, in a system with time-varying parameters, a single forgetting factor remains a challenging issue for the accurate implementation of system identification. The PFFRLS algorithm can adaptively adjust the value of the forgetting factor, according to the residual of the terminal voltage, which has a better recognition effect.

4.2.2 BBDST operating condition

The Beijing bus dynamic stress test (BBDST) experiment is conducted using the statistical method of power battery dynamic test conditions based on actual vehicle operation data. A complete BBDST test includes five working steps of start, acceleration, coasting, braking, and rapid acceleration, which takes 300 s. The battery was tested under BBDST operating condition for 140 times.

Compared with the HPPC operating condition, the BBDST operating condition was conducted under a relatively complicated operating condition. We still select the single forgetting factor λ as 0.99, 0.98, and 0.97, respectively. Figure 6 dedicates the experimental results of the FFRLS algorithm ($\lambda = 0.99$) and the PFFRLS algorithm under BBDST operating condition.

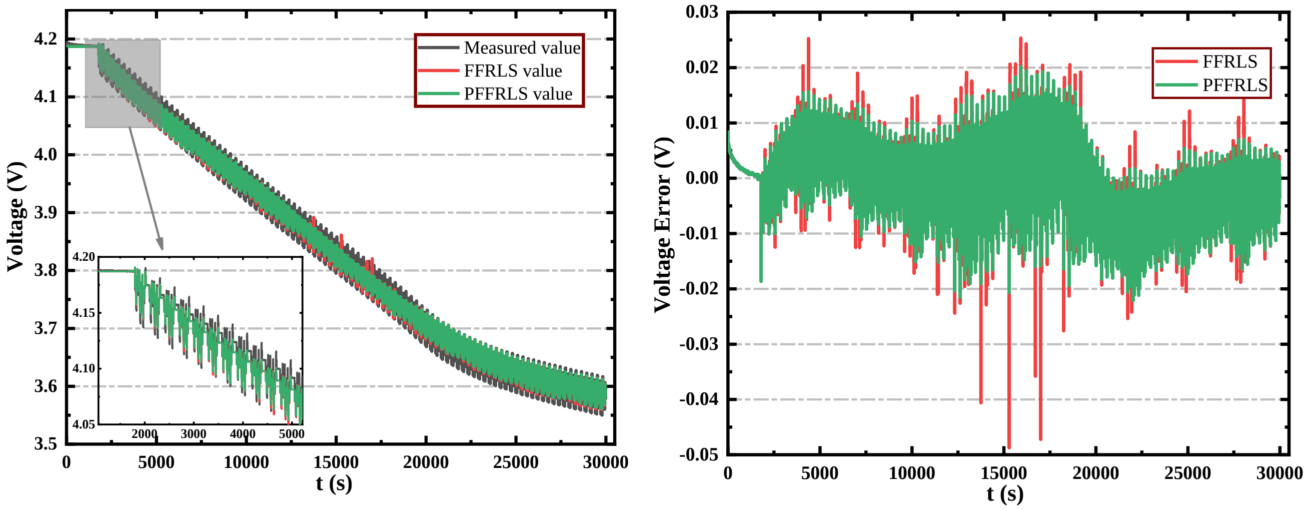

(a) Terminal voltage estimation results (b) Terminal voltage estimation errors

Figure 6. Identification results

The accuracy of the ECM is analyzed by comparing the error between the estimated terminal voltage output and the actual value. Maximum Absolute Error (MaxAE), Mean Absolute Error (MAE) and Root Mean Square Error (RMSE) metrics are shown in Table 5.

Table 5. Error discussion of identification results

Identification method	MaxAE (%)	MAE (%)	RMSE (%)
Single forgetting factor ($\lambda = 0.99$)	4.874	1.450	1.291
Single forgetting factor ($\lambda = 0.98$)	8.435	1.648	2.130
Single forgetting factor ($\lambda = 0.97$)	17.175	2.210	6.501
PFFRLS	1.756	0.610	1.210

From Figure 6 and Table 5, the accuracy of the PFFRLS algorithm is better than the FFRLS algorithm with a single forgetting factor under the BBDST operating condition. The MaxAE, MAE and RMSE of the PFFRLS algorithm are 1.756%, 0.610% and 1.210%, respectively, with the smallest error. Moreover, the error of the single forgetting factor increases as the forgetting factor decreases. The identification process of each parameter for the ECM based on the PFFRLS algorithm is shown in Figure 7.

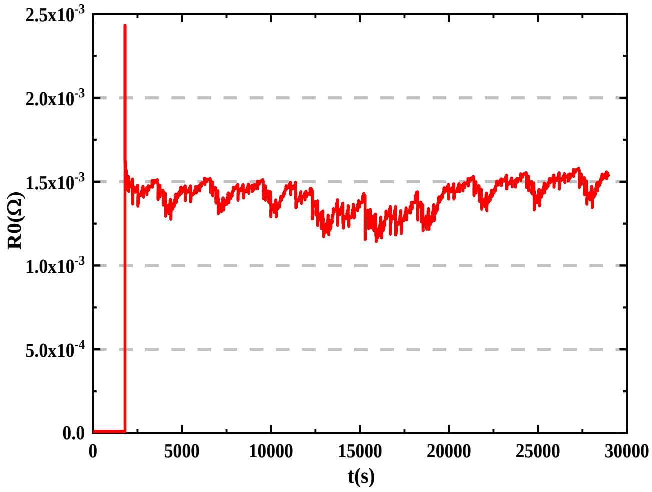

(a) R_0 change curve

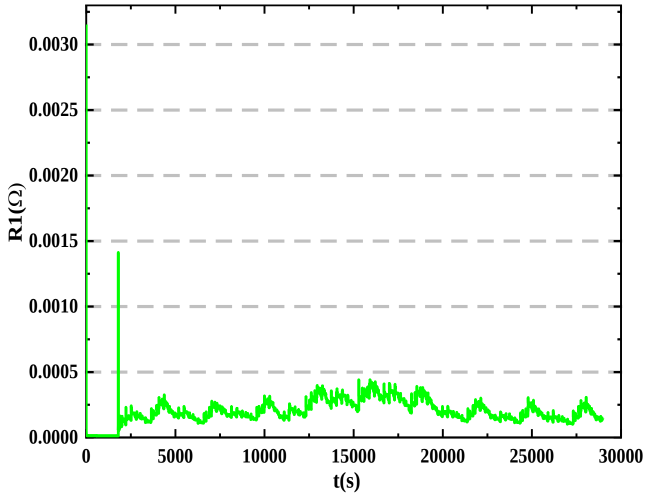

(b) R_1 change curve

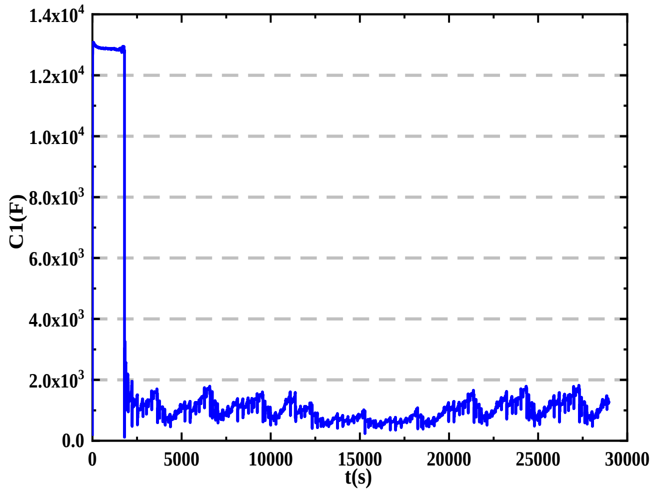

(c) C_1 change curve

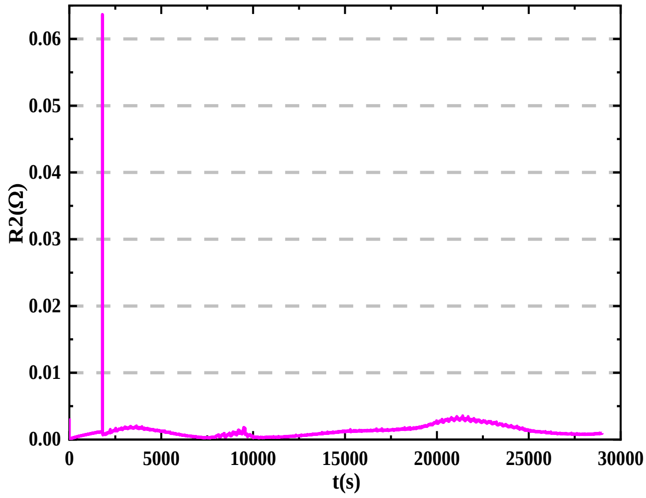

(d) R_2 change curve

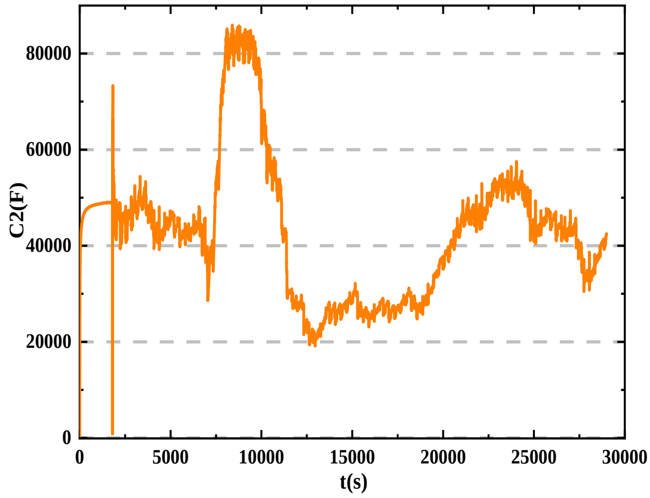

(e) C_2 change curve

Figure 7. The identification process of each parameter

Figure 7 indicates that the PFFRLS algorithm can quickly follow the real-time changes of model parameters and effectively achieve accurate model identification under the BBDST operating condition. The experiment shows that the established ECM has high accuracy and can better reflect the output characteristics of lithium-ion batteries.

4.3 Battery SOC estimation results

4.3.1 SOC estimation under HPPC operating condition

This subsection validates the effectiveness of the proposed algorithm for the battery SOC estimation under HPPC operating condition at 15℃, 25℃ and 35℃, respectively. Among them, the initial value of SOC was set to the correct value (100%). Comparison is made among FFRLS-AEKF ($\lambda = 0.98$) algorithm, PFFRLS-AEKF algorithm, FFRLS-ECC-AEKF ($\lambda = 0.98$) algorithm and PFFRLS-ECC-AEKF algorithm. The SOC estimation results are shown in Figure 8.

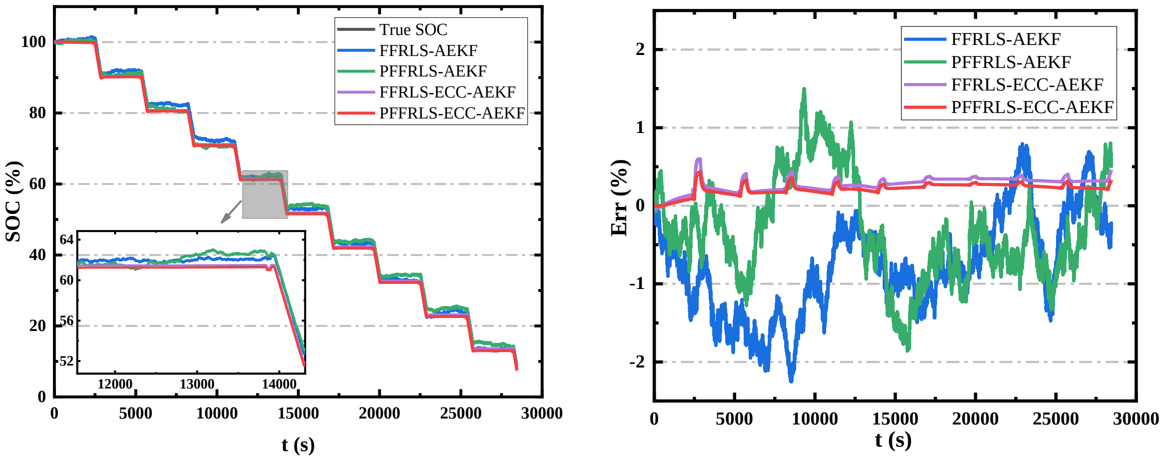

(a) SOC estimated change curves under HPPC at 15℃ (b) SOC estimation errors under HPPC at 15℃

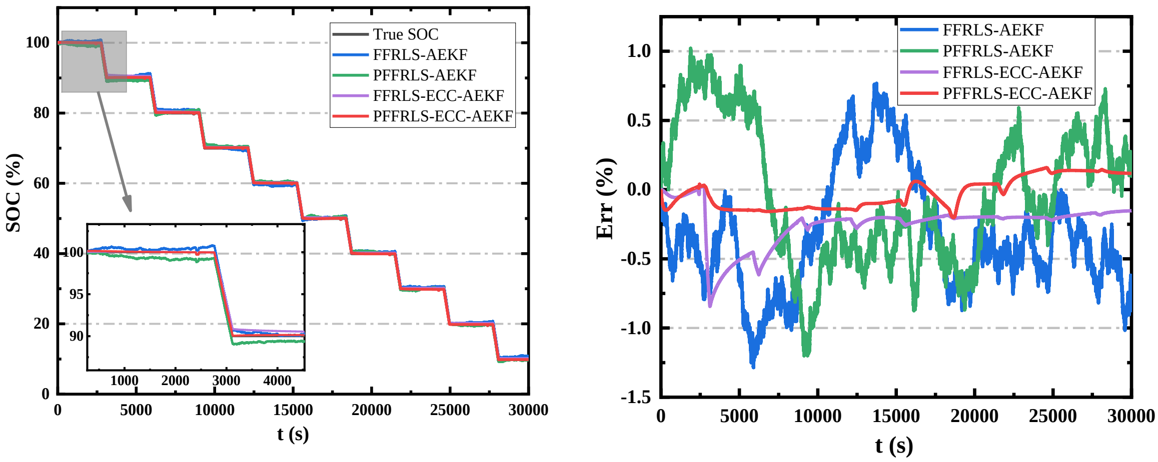

(c) SOC estimated change curves under HPPC at 25℃ (d) SOC estimation errors under HPPC at 25℃

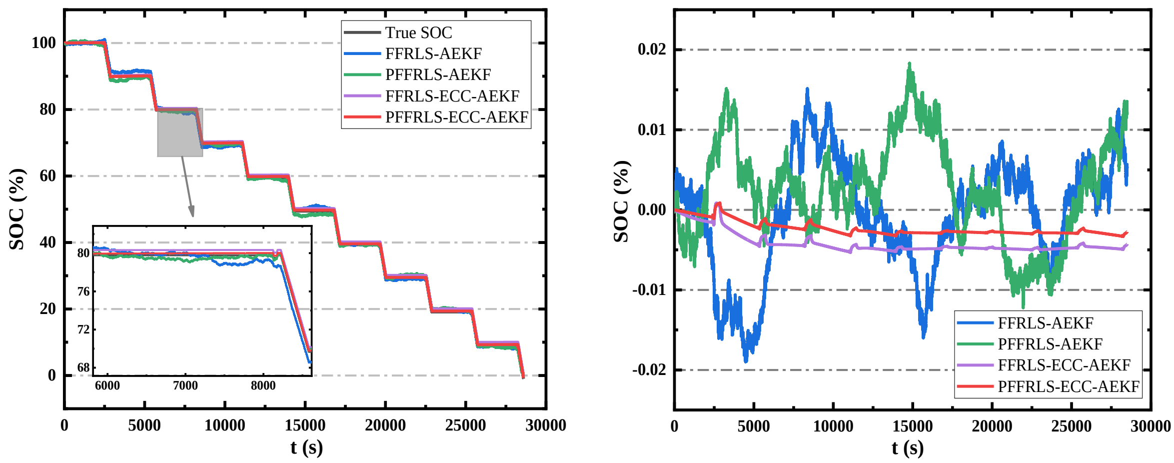

(e) SOC estimated change curves under HPPC at 35°C (f) SOC estimation errors under HPPC at 35°C

Figure 8. SOC estimation results under HPPC operating condition

To assess the performance of the SOC estimation methods more intuitively, the four algorithms are evaluated using MaxAE, MAE, RMSE and time cost (TC). The error properties corresponding to the four methods are detailed in Table 6.

Table 6. Performance evaluation of the SOC estimation methods

Estimation method	Temperature (°C)	MaxAE (%)	MAE (%)	RMSE (%)	TC (s)
	15	2.25	0.85	1.00	2.1687
FFRLS-AEKF (λ =0.98)	25	1.29	0.49	0.55	2.1108
	35	1.81	0.56	0.72	2.3202
	15	1.86	0.62	0.73	2.0018
PFFRLS-AEKF	25	1.20	0.43	0.49	1.9773
	35	1.82	0.52	0.65	2.1288
	15	0.60	0.27	0.29	1.9692
FFRLS-ECC-AEKF (λ =0.98)	25	0.84	0.24	0.28	1.8106
	35	0.52	0.41	0.43	1.5233
	15	0.43	0.21	0.23	1.5167
PFFRLS-ECC-AEKF	25	0.17	0.18	0.11	1.8941
	35	0.20	0.21	0.15	1.7552

From Figure 8, under the HPPC operating condition at 15°C, 25°C and 35°C, respectively, the proposed algorithm not only converges to approximately 0 at the fastest speed but also has a good following degree of the estimated curve. The SOC estimation curve is almost coincident with the true SOC curve and has good stability. The AEKF algorithm performs noise adaptation based on the EKF algorithm, which has large randomness and instability for the battery SOC estimation du e to the influence of noise characteristics. The ECC-AEKF algorithm re-adjusts the priori error covariance, which both avoids the effect of noisy characteristics and reduces the effect of inappropriate error covariance on the priori estimation, and uses the state information from the previous moment to correct the current value for a more appropriate Kalman gain, so as to conduct accurate and robust SOC estimation. In addition, compared to the FFRLS method, the PFFRLS method is able to obtain more accurate ECM parameters to improve the accuracy and stability of the battery SOC estimation. Because of its ability that adaptively adjusts the forgetting degree of historical data. Furthermore, as the temperature decreases/increases, the electrochemical reactions, capacity and discharge voltage inside the battery change, which will affect the accuracy and robustness of the SOC estimation. From Figure 8, the SOC estimation errors of all four algorithms increase in varying degrees at 15°C and 35°C. However, the proposed algorithm still ensures better estimation accuracy and stability compared to the other comparison algorithms.

From Table 6, The MaxAE, MAE and RMSE values of the proposed algorithm are 0.43%, 0.21% and 0.23% at 15°C, 0.17%, 0.18% and 0.11% at 15°C, 0.20%, 0.21% and 0.15% at 35°C, respectively, which are the lowest among the four algorithms. From the TC values, the proposed algorithm increases the accuracy and stability with little increase in the computational effort of the algorithm, which has a lower TC value compared to the AEKF algorithm with the addition of the Sage-Husa adaptive filter.

4.3.2 SOC estimation under BBDST operating condition

This subsection validates the effectiveness of the proposed algorithm for the battery SOC estimation under BBDST operating condition at 15°C, 25°C and 35°C, respectively. The BBDST operating condition is little more complex than the HPPC operating condition. Therefore, it can verify the feasibility of the proposed algorithm in complex conditions. The initial value of SOC was set to the correct value (100%). The algorithms used for comparison are the same as those in section 4.3.1. The SOC estimation results of the lithium-ion battery are shown in Figure 9.

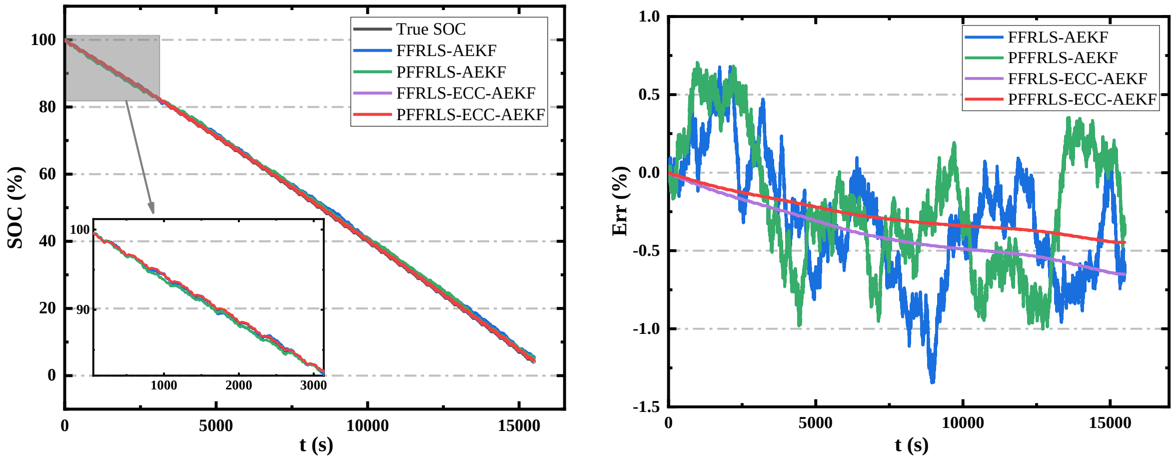

(a) SOC estimated change curves under BBDST at 15°C

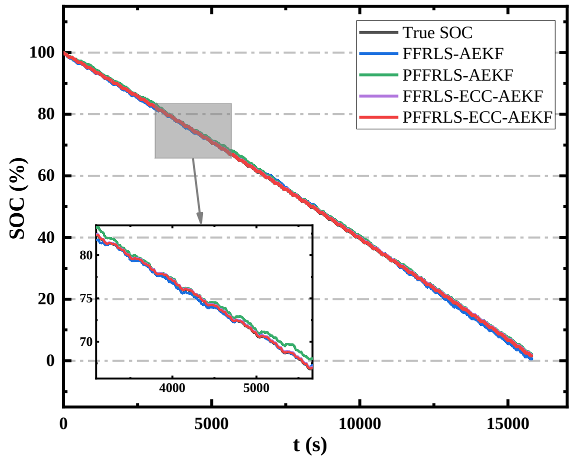

(b) SOC estimation errors under BBDST at 15°C

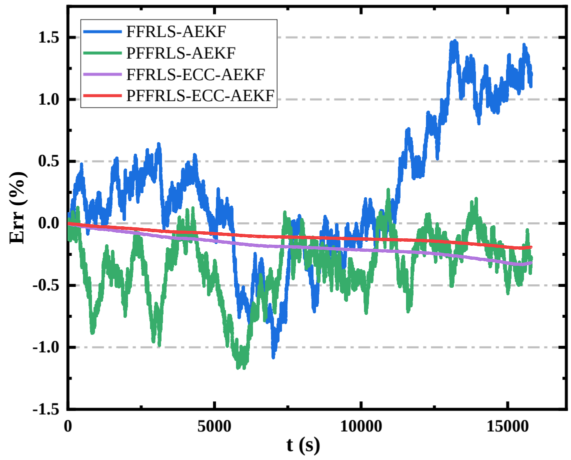

(c) SOC estimated change curves under BBDST at 25°C

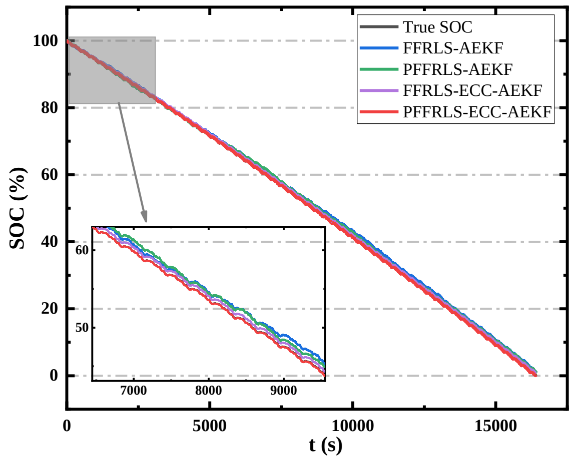

(d) SOC estimation errors under BBDST at 25°C

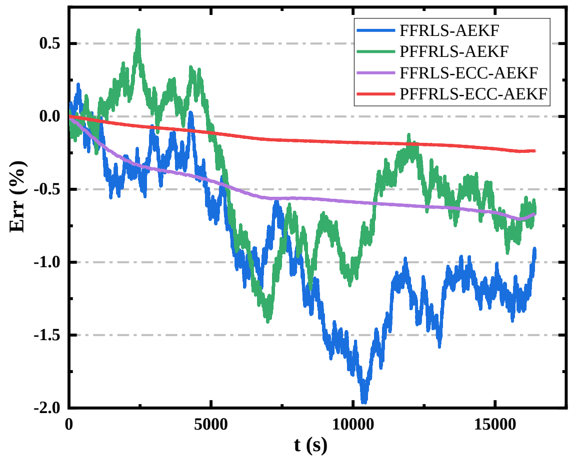

(e) SOC estimated change curves under BBDST at 35°C

(f) SOC estimation errors under BBDST at 35°C

Figure 9. SOC estimation results under BBDST operating condition

In BBDST operating condition at 15°C, 25°C and 35°C, the error properties corresponding to the four methods are presented in Table 7.

Table 7. SOC estimation error properties

Estimation method	Temperature (°C)	MaxAE (%)	MAE (%)	RMSE (%)	TC (s)
	15	1.35	0.41	0.50	1.1688
FFRLS-AEKF (λ =0.98)	25	1.47	0.47	0.62	1.4983
	35	1.96	0.91	1.04	1.2265
	15	1.00	0.40	0.47	1.1776
PFFRLS-AEKF	25	1.17	0.36	0.44	1.4831
	35	1.41	0.55	0.64	1.6166
	15	0.65	0.39	0.42	0.8480
FFRLS-ECC-AEKF (λ =0.98)	25	0.33	0.18	0.2	0.8136
	35	0.71	0.50	0.53	0.9278

	15	0.45	0.27	0.30	0.8475
PFFRLS-ECC-AEKF	25	0.20	0.11	0.12	0.8721
	35	0.24	0.15	0.16	0.9236

From Figure 9, the PFFRLS-ECC-AEKF method still has good estimation results under BBDST operating conditions, which is almost close to the true SOC curve and has better accuracy and stability. Although the estimation errors of the four methods gradually increase with time, the proposed method still converges to a certain value that is close to zero and has better estimation results compared to the other comparison methods. In addition, due to the effect of lower or higher temperatures on the battery activity at 15°C and 35°C, resulting in the accuracy and stability of the battery SOC estimation were slightly reduced. Although the estimation results of the four methods were affected to varying degrees, the overall results remained positive, especially the PFFRLS-ECC-AEKF method performed the best among the four estimation methods. From Table 7, the MaxAE, MAE and RMSE of the PFFRLS-ECC-AEKF method are all less than 0.45%, 0.27% and 0.30%, respectively. The proposed method has not only the lowest error properties of the four battery SOC estimation methods but also the lowest TC value, which combines both high accuracy and low computational effort.

4.3.3 SOC estimation under DST operating condition

This subsection validates the effectiveness of the proposed algorithm for estimating the battery SOC under dynamic stress test (DST) operating condition at 15°C, 25°C and 35°C, respectively. The DST operating condition is a simplified dynamic driving test profile according to the Federal Urban Driving Schedule (FUDS) operating condition, which is widely used in the driving cycle testing of batteries, vehicle performance evaluation, control strategies, etc. The DST operating condition test for the lithium-ion battery in this research has 84 cycles, and the battery SOC varies from 1 to 0.1.

The initial value of SOC was set to the correct value (100%). The algorithms used for comparison are the same as those in section 4.3.1. The SOC estimation results of the lithium-ion batteries are shown in Figure 10.

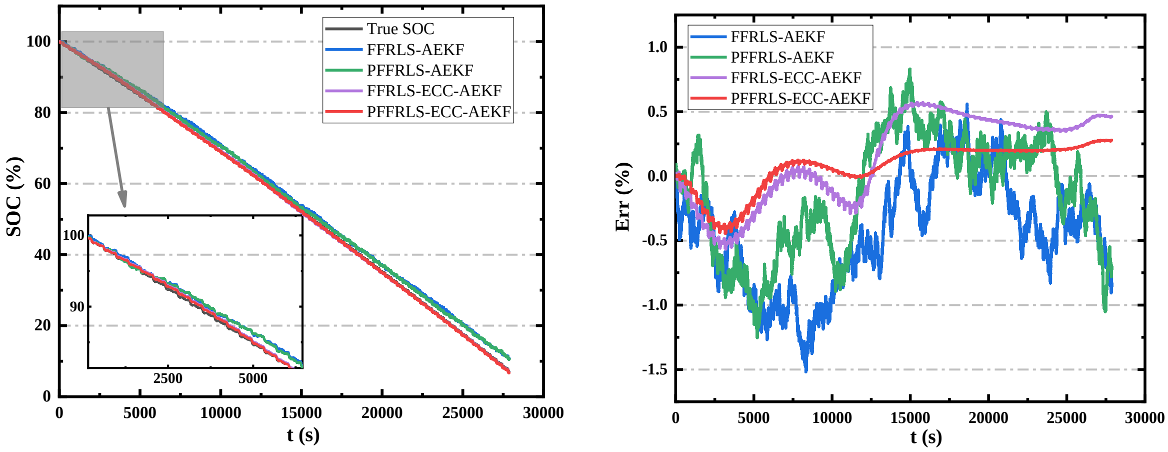

(a) SOC estimated change curves under DST at 15℃

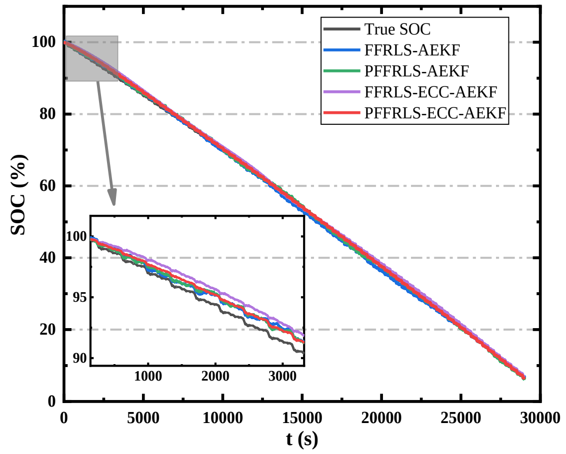

(b) SOC estimation errors under DST at 15℃

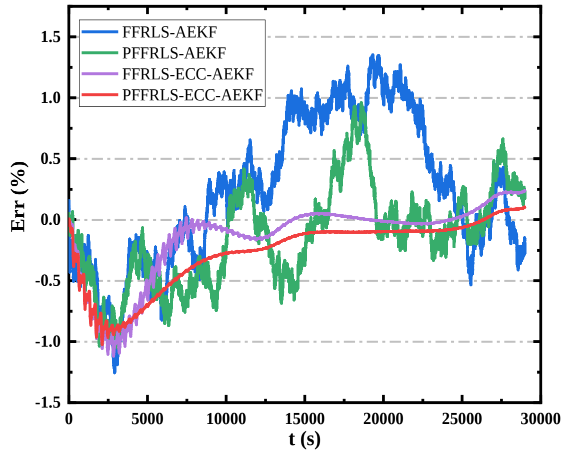

(c) SOC estimated change curves under DST at 25℃

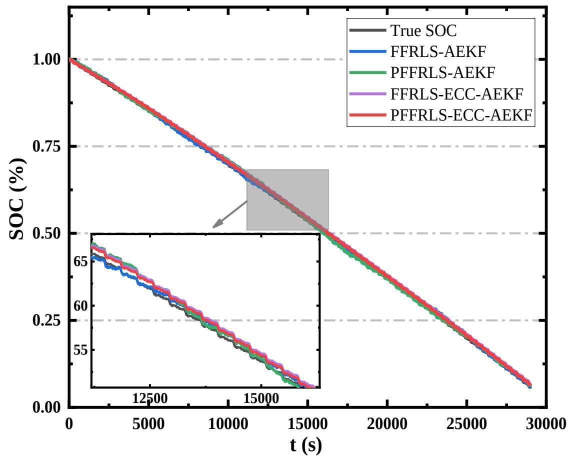

(d) SOC estimation errors under DST at 25℃

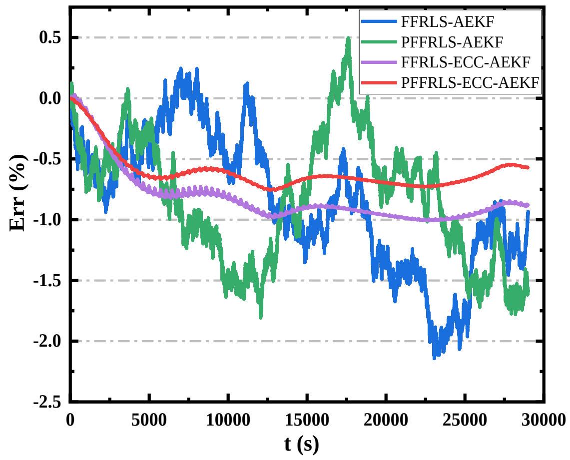

(e) SOC estimated change curves under DST at 35℃

(f) SOC estimation errors under DST at 35℃

Figure 10. SOC estimation results under DST operating condition

Under DST operating condition at 15℃, 25℃ and 35℃, the error properties corresponding to the four algorithms are shown in Table 8.

Table 8. Performance evaluation of the SOC estimation methods

Estimation method	Temperature (℃)	MaxAE (%)	MAE (%)	RMSE (%)	TC (s)
	15	1.56	0.78	0.82	0.9834
FFRLS-AEKF (λ =0.98)	25	1.32	0.63	0.74	1.1448
	35	2.14	0.86	1.02	1.3156
	15	1.39	0.57	0.67	2.0021
PFFRLS-AEKF	25	1.23	0.54	0.65	1.2969
	35	1.81	0.85	0.98	1.4514
	15	0.7	0.57	0.58	0.9975
FFRLS-ECC-AEKF (λ =0.98)	25	1.12	0.25	0.35	0.804
	35	0.10	0.81	0.63	0.9510

	15	0.52	0.37	0.38	0.8344
PFFRLS-ECC-AEKF	25	0.97	0.20	0.310	0.8781
	35	0.76	0.61	0.63	0.8205

From Figure 10, the four battery SOC estimation methods have the best estimation results at 25°C compared to 15°C and 35°C. Temperature affects the battery SOC estimation to some extent. Therefore, a good SOC estimation method should be able to adapt to different ambient temperatures and have good accuracy and stability. At ambient temperature of 25°C, the estimation error of the PFFRLS-ECC-AEKF method gradually decreases with time, and the error curve converges quickly to zero. The estimated results are better than other comparison methods. Although the SOC estimation errors of the four methods gradually increase with time at 15°C and 35°C, the overall effects remain positive. The proposed method performs well among the four SOC estimation methods, which is gradually adapting to changes in ambient temperature and following the true SOC value as soon as possible, with better accuracy and stability.

From Table 8, the error properties of four SOC estimation methods increase to varying degrees compared to the HPPC operating condition and the BBDST operating condition due to the increase in the complexity of the conditions and the number of cycling steps. However, the MaxAE, MAE and RMSE of the PFFRLS-ECC-AEKF method all are less than 0.97%, 0.61% and 0.63% at different temperature, respectively, and have a low TC value.

4.3.4 Comparison with other existing methods

In this subsection, for examining the superiority of the PFFRLS-ECC-AEKF algorithm, the proposed algorithm is compared with the PFFRLS-DEKF algorithm [55], the PFFRLS-AUKF algorithm [56], the PFFRLS-CKF algorithm [57] and the PFFRLS-PF algorithm [58] under HPPC operating condition at 15°C, 25°C and 35°C, respectively, with the initial value of SOC being the correct value (100%). The SOC estimation results of the lithium-ion battery are shown in Figure 11.

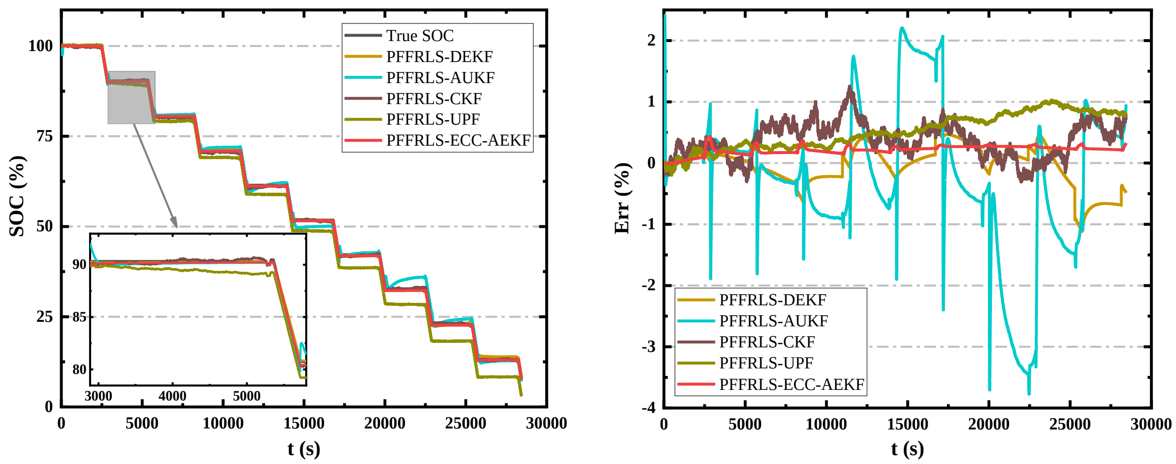

(a) SOC estimated change curves under HPPC at 15℃ (b) SOC estimation errors under HPPC at 15℃

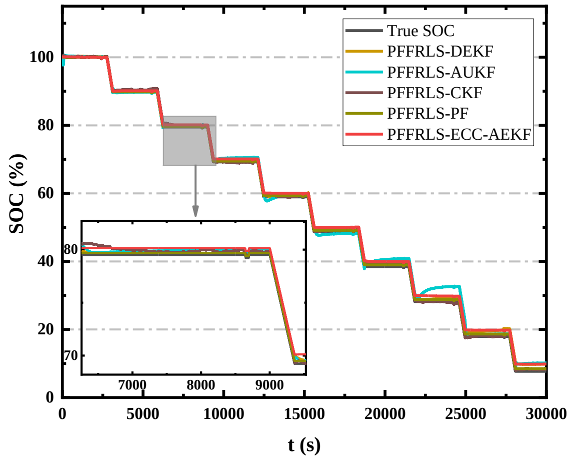

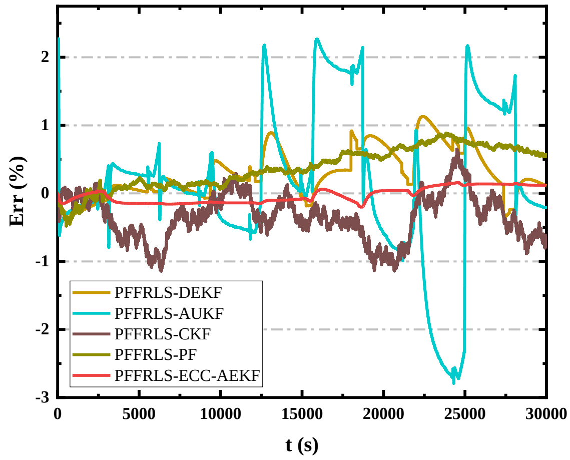

(c) SOC estimated change curves under HPPC at 25℃ (d) SOC estimation errors under HPPC at 25℃

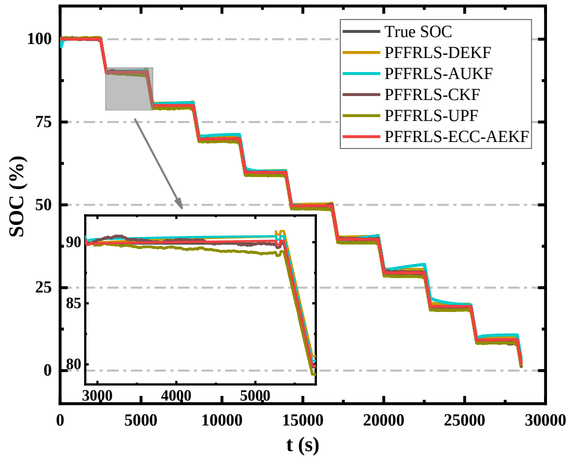

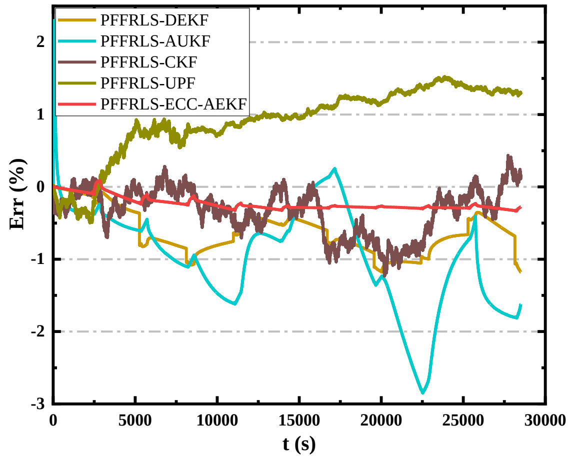

(e) SOC estimated change curves under HPPC at 35℃ (f) SOC estimation errors under HPPC at 35℃

Figure 11. Comparison results of SOC with different filtering algorithms

Under HPPC operating condition at 15℃, 25℃ and 35℃, the error properties corresponding to the five methods are listed in Table 9.

Table 9. Performance evaluation of the SOC estimation methods

Estimation method	Temperature (℃)	MaxAE (%)	MAE (%)	RMSE (%)	TC (s)
	15	1.12	0.25	0.33	3.1243
PFFRLS-DEKF	25	1.13	0.36	0.46	2.9972
	35	1.18	0.62	0.69	3.0233
	15	3.74	0.88	1.22	8.7395
PFFRLS-AUKF	25	2.78	0.80	1.12	8.1773
	35	2.83	0.98	1.19	7.9834
	15	1.25	0.4	0.47	2.4142
FFRLS-CKF	25	1.14	0.36	0.46	2.8154
	35	1.23	0.39	0.48	2.3608

	15	1.02	0.51	0.57	9.1755
PFFRLS-PF	25	0.88	0.41	0.48	8.2502
	35	1.50	0.95	1.02	8.8657
	15	0.43	0.21	0.23	1.5167
PFFRLS-ECC-AEKF	25	0.17	0.18	0.11	1.8941
	35	0.20	0.21	0.15	1.7552

From Figure 11, the five battery SOC estimation methods have the best estimation results at 25°C compared to 15°C and 35°C. Besides, the PFFRLS-AUKF further biasing the SOC estimation results due to the random selection of the sigma that leads to a bias in the mean and covariance of the output near the discontinuity. The PFFRLS-PF is a little better than PFFRLS-AUKF in terms of SOC estimation, but the importance sampling of PF leads to a huge amount of computation. Sacrificing computational power for only a small improvement in accuracy, it is clear that PFFRLS-PF is not suitable for practical applications. The PFFRLS-DEKF and PFFRLS-CKF have better estimation accuracy and stability than the above two methods. However, the PFFRLS-ECC-AEKF has the best SOC estimation effect, with an estimation curve that almost coincides with the true SOC curve and an error curve that converges to approximately zero as soon as possible. In addition, the SOC estimation effect of each method is affected in varying degrees as the temperature decreases or increases. Of these, the PFFRLS-AUKF and the PFFRLS-PF are most affected by temperature change, and the PFFRLS-DEKF and the PFFRLS-CKF are only second to the two above. However, the accuracy and stability of the proposed algorithm are less affected by temperature change. The estimated values of the proposed method can still track the change of the true SOC value as the temperature increases or decreases, which can provide better temperature adaptation and estimation effects compared to other methods.

From Table 9, the PFFRLS-AUKF and the PFFRLS-PF have the highest error properties, while the PFFRLS-DEKF and the PFFRLS-CKF have more optimistic error properties and better estimation results than the two above. It is noteworthy that the proposed algorithm obtains the best estimates at the most optimistic TC value, with MaxAE, MAE and RMSE values all less than 0.43%, 0.21% and 0.23% at three temperatures, respectively.

5 Conclusion

Considering realistic issues such as economic cost, computational cost and overall effectiveness, It is crucial to balance the traditional algorithms and optimal algorithms so that the optimal algorithms are also applicable to practical vehicle applications. In this paper, the widely used EKF is optimized and a new priori error covariance is obtained by mathematical derivation, and then a novel ECC-AEKF is proposed. The ECC-AEKF can not only minimizes the estimation error and reduces the effect of process noise characteristics and inappropriate error covariances on priori estimation, but also adaptively select the priori error covariance according to the estimation effect. Thus, a more suitable Kalman gain was obtained for better battery SOC estimation. Meanwhile, considering that a fixed forgetting factor will lead to reduce the accuracy, stability and topicality of the parameter identification. A PFFRLS method is presented for model parameter identification to adaptively adjust the forgetting level of historical data, which uses error feedback for real-time adaptive selection of the forgetting factor based on the principle of integral separation. Ultimately, the PFFRLS-ECC-AEKF is used for accurate and robust SOC estimation. The accuracy, efficiency and robustness of the proposed method are evaluated using HPPC, BBDST and DST operating conditions at different ambient temperatures, and a comparative analysis of the proposed method with commonly used SOC estimation methods is carried out. The results prove that the PFFRLS-ECC-AEKF achieves higher accuracy with less computation time than other commonly used SOC methods under different ambient temperatures and operating conditions. The MaxAE, MAE and RMSE are all less than 0.97%, 0.032% and 0.33%, respectively. Under DST operating conditions with an initial error of 20%, the proposed algorithm still tracks and converges quickly with an RMSE of less than 1.76%. The PFFRLS-ECC-AEKF has the advantages of simplicity of use, low computational effort and good stability of the EKF, as well as the advantages of high accuracy and robustness of the optimization method. Therefore, the proposed method can bring the possibility of obtaining more accurate SOC estimates for practical applications.

Acknowledgments

The work is supported by the National Natural Science Foundation of China (No. 62173281).

References

[1]. Hassan, M.U., et al., A comprehensive review of battery state of charge estimation techniques. Sustainable Energy Technologies Assessments, 2022. **54**: p. 102801.

[2]. Sulaiman, N., et al., A review on energy management system for fuel cell hybrid electric vehicle: Issues and challenges. Renewable and Sustainable Energy Reviews, 2015. **52**: p. 802-814.

[3]. Espedal, I.B., et al., Current trends for state-of-charge (SoC) estimation in lithium-ion battery electric vehicles. Energies, 2021. **14**(11): p. 3284.

[4]. How, D.N., et al., State of charge estimation for lithium-ion batteries using model-based and data-driven methods: A review. Ieee Access, 2019. **7**: p. 136116-136136.

[5]. Meng, J., et al., Overview of lithium-ion battery modeling methods for state-of-charge estimation in electrical vehicles. Applied sciences, 2018. **8**(5): p. 659.

[6]. Pradhan, S.K. and B. Chakraborty, Battery management strategies: An essential review for battery state of health monitoring techniques. Journal of Energy Storage, 2022. **51**: p. 104427.

[7]. Laadjal, K. and A.J.M. Cardoso, Estimation of lithium-ion batteries state-condition in electric vehicle applications: issues and state of the art. Electronics, 2021. **10**(13): p. 1588.

[8]. Wang, Z., et al., A review on online state of charge and state of health estimation for lithium-ion batteries in electric vehicles. Energy Reports, 2021. **7**: p. 5141-5161.

[9]. Beck, D., et al., Inhomogeneities and cell-to-cell variations in lithium-ion batteries, a review. Energies, 2021. **14**(11): p. 3276.

[10]. Zhang, R., et al., A study on the open circuit voltage and state of charge characterization of high capacity lithium-ion battery under different temperature. Energies, 2018. **11**(9): p. 2408.

[11]. Gold, L., et al., Probing lithium-ion batteries' state-of-charge using ultrasonic transmission–Concept and laboratory testing. Journal of Power Sources, 2017. **343**: p. 536-544.

[12]. Zhang, M. and X. Fan, Review on the state of charge estimation methods for electric vehicle battery. World Electric Vehicle Journal, 2020. **11**(1): p. 23.

[13]. Yu, Q.-Q., et al., A comparative study on open circuit voltage models for lithium-ion batteries. Chinese Journal of Mechanical Engineering, 2018. **31**(1): p. 1-8.

[14]. Yang, K., Y. Tang, and Z. Zhang, Parameter identification and state-of-charge estimation for lithium-ion batteries using separated time scales and extended kalman filter. Energies, 2021. **14**(4): p. 1054.

[15]. Sun, D., et al., State of charge estimation for lithium-ion battery based on an Intelligent Adaptive Extended Kalman Filter with improved noise estimator. Energy, 2021. **214**: p. 119025.

[16]. Li, W., et al., The multi-innovation extended Kalman filter algorithm for battery SOC estimation. Ionics, 2020. **26**: p. 6145-6156.

[17]. Jiang, C., et al., A state-of-charge estimation method of the power lithium-ion battery in complex conditions based on adaptive square root extended Kalman filter. Energy, 2021. **219**: p. 119603.

[18]. Zhang, S., X. Guo, and X. Zhang, An improved adaptive unscented kalman filtering for state of charge online estimation of lithium-ion battery. Journal of energy storage, 2020. **32**: p. 101980.

[19]. Kai, W., et al., State of charge (SOC) estimation of lithium-ion battery based on adaptive square root unscented kalman filter. International Journal of Electrochemical Science, 2020. **15**(9): p. 9499-9516.

[20]. Feng, J., et al., An adaptive state of charge estimation method of lithium-ion battery based on residual constraint fading factor unscented Kalman filter. Ieee Access, 2022. **10**: p. 44549-44563.

[21]. Tian, Y., et al., A combined method for state-of-charge estimation for lithium-ion batteries using a long short-term memory network and an adaptive cubature Kalman filter. Applied Energy, 2020. **265**: p. 114789.

[22]. Zhang, A., et al., A novel strong tracking cubature Kalman filter and its application in maneuvering target tracking.

Chinese Journal of Aeronautics, 2019. **32**(11): p. 2489-2502.

[23]. Wang, Y. and Z. Chen, A framework for state-of-charge and remaining discharge time prediction using unscented particle filter. Applied Energy, 2020. **260**: p. 114324.

[24]. Chen, N., et al., Estimating the state-of-charge of lithium-ion battery using an H-infinity observer based on electrochemical impedance model. Ieee Access, 2020. **8**: p. 26872-26884.

[25]. Chen, M., et al., Sliding Mode Observer for State-of-Charge Estimation Using Hysteresis-Based Li-Ion Battery Model. Energies, 2022. **15**(7): p. 2658.

[26]. Shrivastava, P., et al., Overview of model-based online state-of-charge estimation using Kalman filter family for lithium-ion batteries. Renewable Sustainable Energy Reviews, 2019. **113**: p. 109233.

[27]. Liu, Z., et al., A Combined State of Charge Estimation Method for Lithium‐Ion Batteries Using Cubature Kalman Filter and Least Square with Gradient Correction. Advanced Theory Simulations, 2022. **5**(3): p. 2100331.

[28]. Takyi‐Aninakwa, P., et al., A strong tracking adaptive fading‐extended Kalman filter for the state of charge estimation of lithium‐ion batteries. International Journal of Energy Research, 2022. **46**(12): p. 16427-16444.

[29]. Lai, X., et al., Capacity estimation of lithium-ion cells by combining model-based and data-driven methods based on a sequential extended Kalman filter. Energy, 2021. **216**: p. 119233.

[30]. Wei, Z., et al., Noise-immune model identification and state-of-charge estimation for lithium-ion battery using bilinear parameterization. IEEE Transactions on Industrial Electronics, 2020. **68**(1): p. 312-323.

[31]. Lipu, M.H., et al., Data-driven state of charge estimation of lithium-ion batteries: Algorithms, implementation factors, limitations and future trends. Journal of Cleaner Production, 2020. **277**: p. 124110.

[32]. Zhang, G., B. Xia, and J. Wang, Intelligent state of charge estimation of lithium-ion batteries based on LM optimized back-propagation neural network. Journal of Energy Storage, 2021. **44**: p. 103442.

[33]. Lian, G., et al., Considering the temperature influence state‐of‐charge estimation for lithium‐ion batteries based on a back propagation neural network and improved unscented Kalman filtering. International Journal of Energy Research, 2022. **46**(13): p. 18192-18211.

[34]. Chandran, V., et al., State of charge estimation of lithium-ion battery for electric vehicles using machine learning algorithms. World Electric Vehicle Journal, 2021. **12**(1): p. 38.

[35]. Ma, L., C. Hu, and F. Cheng, State of charge and state of energy estimation for lithium-ion batteries based on a long short-term memory neural network. Journal of Energy Storage, 2021. **37**: p. 102440.

[36]. Hannan, M.A., et al., State-of-charge estimation of li-ion battery using gated recurrent unit with one-cycle learning rate policy. IEEE Transactions on Industry Applications, 2021. **57**(3): p. 2964-2971.

[37]. Deng, Z., et al., Data-driven state of charge estimation for lithium-ion battery packs based on Gaussian process regression. Energy, 2020. **205**: p. 118000.

[38]. Li, X., et al., SOC Estimation of Lithium-Ion Battery for Electric Vehicle Based on Deep Multilayer Perceptron. Computational Intelligence Neuroscience, 2022. **2022**.

[39]. Feng, F., et al., Co-estimation of lithium-ion battery state of charge and state of temperature based on a hybrid electrochemical-thermal-neural-network model. Journal of Power Sources, 2020. **455**: p. 227935.

[40]. Vidal, C., et al., Machine learning applied to electrified vehicle battery state of charge and state of health estimation: State-of-the-art. Ieee Access, 2020. **8**: p. 52796-52814.

[41]. Jiao, M., et al., More intelligent and robust estimation of battery state-of-charge with an improved regularized extreme learning machine. Engineering Applications of Artificial Intelligence, 2021. **104**: p. 104407.

[42]. Bian, C., H. He, and S. Yang, Stacked bidirectional long short-term memory networks for state-of-charge estimation of lithium-ion batteries. Energy, 2020. **191**: p. 116538.

[43]. Lipu, M.S.H., et al., State of charge estimation for lithium-ion battery using recurrent NARX neural network model based lighting search algorithm. IEEE access, 2018. **6**: p. 28150-28161.

[44]. Hossain, M., M. Haque, and M.T. Arif, Kalman filtering techniques for the online model parameters and state of

charge estimation of the Li-ion batteries: A comparative analysis. Journal of Energy Storage, 2022. **51**: p. 104174.

[45]. Wang, Y., et al., A comprehensive review of battery modeling and state estimation approaches for advanced battery management systems. Renewable Sustainable Energy Reviews, 2020. **131**: p. 110015.

[46]. Liu, Y., et al., A review of lithium-ion battery state of charge estimation based on deep learning: Directions for improvement and future trends. Journal of Energy Storage, 2022. **52**: p. 104664.

[47]. Wang, Y., et al., A fractional-order model-based state estimation approach for lithium-ion battery and ultra-capacitor hybrid power source system considering load trajectory. Journal of Power Sources, 2020. **449**: p. 227543.

[48]. Sun, F., R. Xiong, and H. He, A systematic state-of-charge estimation framework for multi-cell battery pack in electric vehicles using bias correction technique. Applied Energy, 2016. **162**: p. 1399-1409.

[49]. Ali, M.U., et al., Towards a smarter battery management system for electric vehicle applications: A critical review of lithium-ion battery state of charge estimation. Energies, 2019. **12**(3): p. 446.

[50]. Hu, X., et al., State estimation for advanced battery management: Key challenges and future trends. Renewable and Sustainable Energy Reviews, 2019. **114**: p. 109334.

[51]. Zhou, W., et al., Review on the battery model and SOC estimation method. Processes, 2021. **9**(9): p. 1685.

[52]. Liu, Z., et al., Fractional variable-order calculus based state of charge estimation of Li-ion battery using dual fractional order Kalman filter. Journal of Energy Storage, 2022. **52**: p. 104685.

[53]. Tamilselvi, S., et al., A review on battery modelling techniques. Sustainability, 2021. **13**(18): p. 10042.

[54]. Xu, Y., et al., Accelerate convergence of polarized random Fourier feature-based kernel adaptive filtering with variable forgetting factor and step size. IEEE Access, 2020. **8**: p. 126887-126895.

[55]. Wang, L., et al., State of charge estimation for LiFePO4 battery via dual extended kalman filter and charging voltage curve. Electrochimica Acta
2019. **296**: p. 1009-1017.

[56]. Lin, X., et al., State of charge estimation with the adaptive unscented Kalman filter based on an accurate equivalent circuit model. Journal of Energy Storage, 2021. **41**: p. 102840.

[57]. Peng, J., et al., An improved state of charge estimation method based on cubature Kalman filter for lithium-ion batteries. Applied energy, 2019. **253**: p. 113520.

[58]. Chen, Z., et al., Particle filter-based state-of-charge estimation and remaining-dischargeable-time prediction method for lithium-ion batteries. Journal of Power Sources, 2019. **414**: p. 158-166.